REPORT No
60/1

A STUDY OF THE FLOW THROUGH A VERTICAL AXIS PROPELLER

J. A. McKILLOP

CONTRACT No. NONR - 4525 (00) (X)
ERA PROJECT No. 60

prepared for
DEPARTMENT OF THE NAVY
BUREAU OF SHIPS
FUNDAMENTAL HYDROMECHANICS RESEARCH PROGRAM
SR 009 01 01
ADMINISTERED BY DAVID TAYLOR MODEL BASIN
WASHINGTON 25, D.C.

APRIL 1965

ENGINEERING RESEARCH ASSOCIATES
160 BAY STREET TORONTO CANADA

ENGINEERING RESEARCH ASSOCIATES

A STUDY OF THE FLOW THROUGH A VERTICAL AXIS PROPELLER

by

J.A. McKillop

Contract No. Nonr-4525(00)(X)
ERA Project No. 60

Prepared for

Department of the Navy
Bureau of Ships
Fundamental Hydromechanics Research Program
SR 009 01 01
Administered by the David Taylor Model Basin
Washington 25, D.C.

April 1965

ABSTRACT

The application of a three dimensional flow visualisation technique to the study of the flow pattern of a vertical axis propeller is described. Photographs of the streamlines encountered by a blade throughout a complete orbital cycle are shown and analysed to yield the inflow vector. The results are compared with blade normal force time histories obtained by strain gage readings from one blade root. The computed thrust is finally compared with existing performance data.

CONTENTS

LIST OF CHARTS AND ILLUSTRATIONS

Appendix Figures

1.0 INTRODUCTION

Propeller propulsion systems, using the principle of obtaining lift from blades, are normally designed to operate with an undisturbed flow entering the phase of rotation. The flow conditions encountered by the blades (velocity, angle, etc.) may therefore be predicted with some accuracy. When this is not the case, (i.e. with a pusher propeller) the unpredictable inflow condition may result in severe degradation of performance, as well as vibration due to buffet from unsteady flow components. In the design of a ship, there is no more important single problem to be solved than that of determination of propeller size, shape and number of blades required to minimise unsteady thrust and torque due to the disturbed inflow from the ship's hull.

The situation for the vertical axis propeller, with the axis of rotation normal to the free stream, is unique. In this case, the stream conditions encountered by the upstream blades may be predicted quite well, but the flow passing through the rear blades is completely unpredictable. The propulsive effectiveness of a blade as it completes a full revolution is therefore difficult to calculate. It is possible, of course, to measure the blade forces, but while this approach will yield the actual values for these forces, no real insight is gained into the dynamic fluid conditions which are responsible for the generation of them. Development of configurations of improved performance must consequently be achieved by intuitive design coupled with systematic experimentation.

It is therefore clear that, if expressions could be derived to describe the flow conditions through a vertical axis propeller, design and development of these units could be carried on in a more positive manner. The research program which is the subject of this report is a first step toward the derivation of such expressions. In this work, a flow visualisation technique using a unique facility normally used for low speed aerodynamic studies has been applied to the study of the flow through the cycloidal propeller.

Three different types of flow photograph were made during this program. From each, the flow encountered by a blade throughout its complete cycle can be measured. The spanwise variation of the flow parameters can also be measured, and the load distribution across the blade calculated. The calculated blade load time history is compared to a measured blade load time history as the final step to establish the feasibility of applying this technique to the development of cycloidal propellers.

2.0 EXPERIMENTAL APPARATUS

The technique used in this research program is a method of flow visualisation which permits detailed definition of streamlines. A special facility is used and the flow characteristics are recorded photographically.

2.1 Test Facility.

The facility is the flow visualisation water tunnel of the National Research Council of Canada. This apparatus is a small closed-return tunnel with a rectangular working section; 10" wide by 13" high x 40" long. The bottom and one side wall of the working section are of glass to permit illumination and viewing of the flow. The tunnel has rather a modest performance - up to about 7 ft/sec. Model strength limitations required that the maximum speed be held to less than 2 ft/sec for this program.

A suspension of fine aluminum powder is used as the means of streamline visualisation. The individual particles are extremely light, hence follow a streamline very closely, even when turbulent. The flow is illuminated from the underside by a plane source of light which defines a two dimensional section of the flow field. The complete three dimensional flow pattern may be built up from a series of photographs of these sections. The lamp may be moved to illuminate transverse flow sections which are observed by means of a mirror mounted in the tunnel downstream of the working section. The tunnel is shown in Figs. 5 and 6.

The flow is photographed by different techniques depending on the type of information desired. These are:

1) Long Exposure Still; This records a relatively long particle passage, i.e., a streamline. As the light source operates on alternating current, the streamline is shown as a series of dots. If the light frequency is known, and a known length is included in the photograph , the stream velocity can be calculated from the dot spacing. The direction may also be measured, thus completely defining the stream vector in each plane. This type of photograph is the normal record yielding the most complete information. Turbulent areas can be seen and their limits defined, but a different technique is used if detail of the turbulence is required.

2) Short Exposure Still; This type of photograph defines the concentration of particles caused by vortices within the overall flow. The exposure time is such that each particle is seen only once. This technique is only useful in conjunction with the normal records.

3) Motion Pictures; This type of record is made when it is desired to study some sequence in the flow. The frame rate is varied depending on the timing of the sequences and on whether streamline or short exposure type pictures are required. For direct viewing, it is usually wise to slow the action as much as is possible within the limits of available light and film speed rating.

2.1 Test Model.

The model used in this program was built to a design used by the David Taylor Model Basin for performance experiments. (Model 4571, Propeller 3480.) The design of the outer housing was altered slightly to allow fitment into an existing opening in the rear wall of the tunnel. The internal

design was somewhat simplified to eliminate the flingers of the DTMB model, but the principle of cam operation was retained. The unit had four blades as shown in Figure 1.

The pitch ratio chosen for the model was 0.7π . Blade motion was imposed by small cranks controlled by a cam cut for this pitch ratio as shown below. The blade design was taken from DTMB drawing no. P-4074. The blades were made of transparent material to allow transmission of light across the unit. (Fig. 3) One blade was mounted on a strain gaged spring to measure blade forces, with the signals brought out on slip rings. The complete working unit was sealed and filled with oil to avoid corrosion.

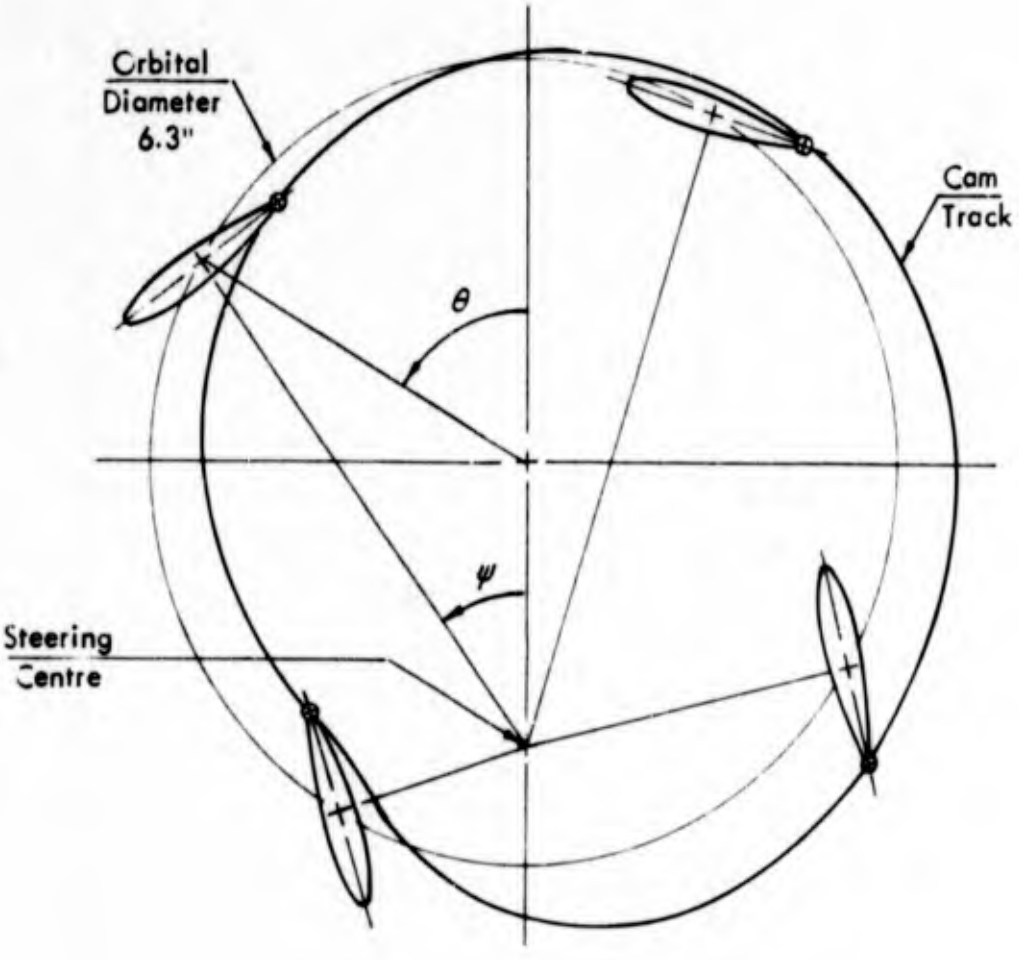

Three types of photograph were required during different phases of the program, two of which required a special camera carrier. (Fig. 2). In this mechanism, the camera lens is aligned with the pitch axis of one blade. The camera is given the same motion as the blade by an identical crank-cam mechanism. The inertia of the camera on its mount, and the high acceleration required over a portion of the cycle generated very high inertia loads. It was necessary to neutralise these loads by counterbalancing the camera assembly. A lead block with the same inertia as the camera assembly was given reverse articulation to eliminate external loads, although internal loading remained high.

The model unit and the camera carrier were chain driven from a common shaft. Keyways for the drive sprockets were milled after the model was assembled and aligned, so that it was possible to disassemble and reassemble the model without recurring alignment problems. The complete model was quite robust as shown in Figure 4. The model is shown installed in the tunnel in Figures 5 and 6. The model could be operated at either 60 or 120 RPM.

The camera used for all motion picture work was a Bolex Model H16 fitted with an f 1.8 lens of 25 mm focal length. When used in the articulated carrier, the camera was operated by a solenoid switch. Conventional still photographs were made with a Bronica "S" single lens reflex camera to obtain a larger negative with extra clarity for enlargement. All photographs for analysis were made on Kodak Plus X negative film, while all documentary footage was made on Kodak Ektachrome ER Type 7257 colour film.

3.0 EXPERIMENTAL PROGRAM

The tests were run in two series. The first was a feasibility test to check operation of the model and to experiment with aluminum powder density, exposure time, lamp flash rate and film type. Following evaluation of these results, the model was modified to improve the photographic coverage and the strain gage spring was made more sensitive. The second series of tests was then made for the taking of test data. There were three separate phases.

3.1 Phase 1.

During this portion of the testing, photographs were made of the overall flow field. The model was operated at 60 RPM. Motion pictures were made for sequence studies and normal streamline stills for detailed flow analysis. Photographs were made for four spanwise sections and two transverse sections as shown below. Both motion pictures and conventional stills were made using relatively long exposures - 1/8 second for the stills and 8 frames/second for motion pictures. The lamp flash rate was 240/second.

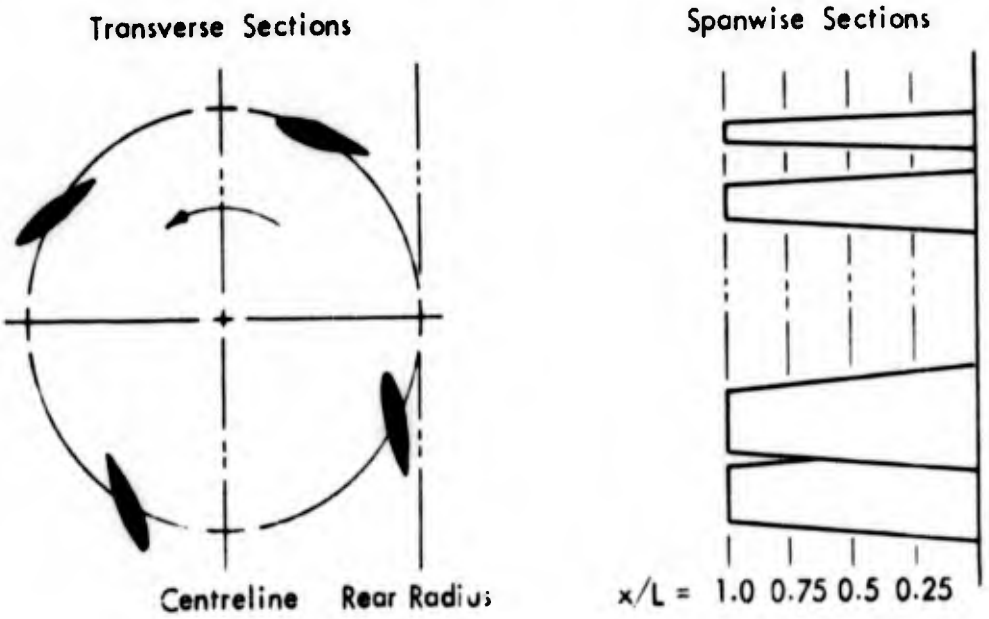

Four values of advance ratio V/ND were selected for study. These were;

J = .554 V/πND = .1766 - the minimum possible.

J = 1.25 V/πND = .4

J = 1.75 V/πND = .56 - the speed for maximum efficiency.

J = 2.25 V/πND = .72 - the speed for zero thrust.

At the low advance ratio, the propeller maintained a steady flow in the tunnel. The latter two advance ratios were selected from DTMB performance curves as flow conditions which merit detailed study. The intermediate value, J = 1.25, was selected to provide continuity of coverage.

After completing the photography of flow sections, the blade forces were recorded for the same four values of advance ratio. The forces were recorded with the propeller operating normally, and with an endplate fitted to make the flow two dimensional.

3.2 Phase II

In this second phase of testing, the rotating camera arrangement was used for photography. The articulation crank/cam drive was disconnected and the camera fixed on a radius. The lens therefore followed the orbital path of the blade, recording the flow relative to the blade pitch axis. Also recorded was the motion of the blade about its pitch axis.

The flow pattern was recorded for the four advance ratios tested in Phase I , and for the four spanwise sections from x/L = 0.25 to x/L = 1.0.

3.3 Phase III .

The third phase of the test made use of the rotating and articulated camera carrier for photography. Thus, the camera recorded the flow relative to the blade chord. Photographs were made of the four spanwise sections at each of the four advance ratios selected in Phase I .

The test program was completed with the calibration of the strain gaged blade, measurement of the blade inertia forces and determination of the blade's natural frequency and damping coefficient.

4.0 RESULTS

The bulk of the test results consists of a very large number of flow photographs, far too many to be reproduced in this report. Samples of each type of photograph are included, however, with the detailed analysis of selected cases given in the next section.

4.1 Phase I

In Figures 7 through 10 are shown a series of typical photographs made in this phase of the test. These figures show the general flow through the propeller cylinder, at the half span section, for the four selected advance ratios. The propeller is rotating counterclockwise, with the flow from left to right.

Samples of transverse section photographs also made during this phase are shown in Figs. 11 to 14. In these views, the propeller is seen from the rear. The blade on the left of the frame is the retreating blade, (it is coming toward the camera), while the blade on the right is advancing (away from the camera).

Strip prints of motion picture film made during this phase, are shown in Figs. 15 and 18. These are made with a comparitively long exposure time to show the streamline sequence. High speed motion pictures were made as well, but are not suitable for printing. They were incorporated into a film version of this report.

Sample strain gage records which were taken at this stage are given in the Appendix. Results for the two dimensional flow case are shown in

Figs. A:6 to A:9, with records for three dimensional flow conditions shown in Figs. A:10 to A:13. The blade load due to inertia (model operating in air) and the natural mode of the blade in water are given in Figs. A:4 and A:5 respectively.

4.2 Phase II

Photographs taken in this phase are all motion pictures. Sample strip photographs of the flow at the half span section are shown in Fig. 16 for $J = .5$ and in Fig. 19 for $J = 1.75$. These photographs are long exposure type showing the streamlines. High speed (short exposure) photographs are included in the film report.

4.3 Phase III

Sample strip prints from the motion pictures taken during this phase of the test are shown in Fig. 17 for $J = .5$ and in Fig. 20 for $J = 1.75$. These are for the section at half span and are the long exposure type. As for the previous phases, the high speed photographs were incorporated into the film report.

The Reynolds Number of the flow, at a model speed of 60 RPM and based on the average blade chord, was somewhat low - $\frac{R\Omega \bar{c} \rho}{\mu} = 12,200$.

5.0 ANALYSIS AND DISCUSSION

5.1 General Flow Studies

The photographs taken during Phase I, (e.g. Figs. 7-10), were analysed to obtain the actual inflow existing at the orbital circle around the complete periphery. The definition of the inflow vector and of other blade operating parameters is given below.

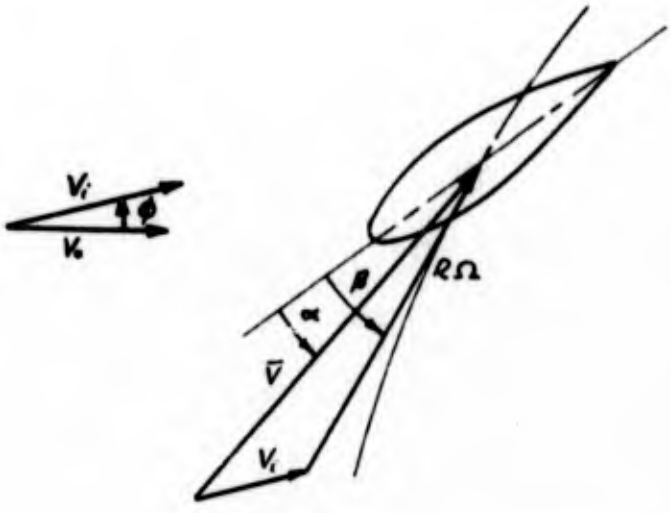

For comparison purposes, the flow parameters for a completely undisturbed inflow are given in Chart 1. Ideally, these conditions would apply over the complete blade span.

In practice, it proved to be impossible to set the tunnel operating conditions at exactly the selected advance ratios. Thus, the actual test conditions, as deduced from the photographs, were;

$J = .556$, $J = 1.28$, $J = 1.804$ and $J = 2.281$.

The actual inflow characteristics for the advance ratio $J = .556$ are given in Chart II as deduced from the flow photographs. The flow is

markedly different from that which is treated by the ideal theory. Over two facing extensive parts of the orbital cycle, from $\theta = 160°$ to $200°$ and from $\theta = 320°$ to $20°$ the flow completely breaks down and becomes turbulent. In the region about $\theta = 180°$, this is doubtlessly due to stalling of the blade at its high angle of attack, followed by the sudden pitch to a reversed high angle of attack. This stall at high incidence and separation due to high angular velocity may be seen in the film version of the report. The reason for the turbulent flow in the region about $\theta = 0°$ is not so clear.

Fortunately, these two areas of disturbed flow occur over regions in which the blade delivers no thrust, even if it were to develop lift. The drag is probably high, however, which would increase the propeller torque.

One very interesting feature of the flow at low advance ratio is the large spanwise component shown of the transverse sections, Figs. 11 and 12. The direction of this component is from the tip toward the root, and has a velocity component comparable to the streamwise component in the same region of the orbital cycle. This spanwise flow may be the cause of the flow breakdown in the region of $\theta = 0°$.

In general, the propeller acts like a nozzle. The inflow is concentrated toward the rotation centre from the upstream side, and is expelled in an expanding flow pattern from the downstream side. As expected, the flow velocities encountered by the blade on the return part of the cycle are higher than those on the upstream part of the cycle, and very much higher than the velocities of the free stream. Consequently, one would expect the blade flow parameters to be quite different from those shown in the ideal curves of Chart 1

and this is seen to be the case.

In Chart III, the blade flow parameters calculated from the measured inflow are shown. The velocity seen by the blade is not changed a great deal as the inflow, even when speeded up by a large factor, is still only a small fraction of the orbital velocity. Notice, however, the drop in velocity in the region $\theta = 180°$ caused by blade stall and resulting turbulence. On the return cycle, the blade flow velocity rises somewhat higher than the idealised value, due to the acceleration from the thrust of the forward blades.

The effective incidence of the blade is very much reduced from the idealised value over most of the cycle, except at the tip station. The blade load will be much less than might be expected, but due to the effective twist caused by the spanwise variation of inflow angle, the load will be shifted toward the tip. For example, a simple calculation of blade load at $\theta = 120°$ shows the lift of the blade to be reduced by 25.5% compared to that due to the idealised flow, while the root bending moment is reduced by only 21.5%.

It is difficult, using the methods given in the Appendix, to calculate the blade load accurately, because of the spanwise variation of velocity as well as angle. Therefore, no comparison of blade load and thrust with the measured values is given for the low advance ratio.

For the advance ratio of maximum efficiency, the perturbations of the inflow are much less, as shown in Chart IV. There is now no clearly separated flow region as existed at lower speed, although the inflow velocity shows a drop near $\theta = 180°$ at the outer span stations, probably due to

the effect of the tip vortex at high blade lift. As might be expected, the inflow velocity is higher over the return portion of the cycle, although it is never more than 20% greater than the free stream speed. Angular deviation from the free stream is also small.

In Figs. 13 and 14, it can be seen that the spanwise flow component has almost disappeared. It might be expected, therefore, that there would be little or no velocity variation across the span, and this is seen to be true.

In Chart V, the blade flow parameters for the measured inflow are given. There is now very little variation in speed across the span. But there is still a significant spanwise variation of incidence, giving an effective twist to the blade, particularly on the return cycle. It is feasible in this case (variation of angle only) to calculate the lift of the blade, using the methods given in the Appendix.

The blade lift time history over a complete cycle is shown in Chart VI. Also shown for comparison is the blade normal force curve derived from the strain gage records for the same case. The agreement is seen to be reasonable except over the final sixty degrees or so, where the strain gage results do not show a high negative load.

Finally, the thrust in the direction of the free stream can be computed for the calculated blade lift time history. The thrust time history is shown in the lower part of Chart VI, for both a single blade and for the total resultant of four blades. The striking feature of the thrust curve is the very high cyclic thrust variation, amounting to $\pm$ 35% of the mean thrust. The

frequency is the frequency of blade passage. One might expect a high vibration level from this high thrust variation, but perhaps it is partially absorbed by blade bending, or the mounting of the unit in the ship.

5.2 Detailed Blade Flow Studies

The photographs made using the rotating camera assembly, both with the radial installation (e.g. Figs 16 and 19), and the articulated unit (Figs 17 and 20), proved to be disappointing for analytical purposes. Nevertheless, these two types of photograph are quite spectacular for direct viewing and do provide some qualitative insight into the mechanism of the flow.

It was initially proposed to calculate the lift coefficient of the blade by analysis of the streamline pattern over the blade surface, but the enlargement required to yield a reasonable print from the 16 mm. negative size destroyed the fine particle definition which is necessary for this technique. The photographs were analysed to yield the angle of attack of the blade and the stream velocity seen by the blade, and these results are shown in Chart VII, together with the same flow parameters developed in the previous section given on Chart V.

It is evident that the scatter in these results is rather high and they must be regarded as unreliable. The velocity results from the articulated camera photographs show the effect of blade angular motion at $\theta = 180°$, an effect which is not apparent from the other two types of photograph. But this is not particularly important as the blade is not generating thrust over this region.

The principal value of the photographs made with the moving camera carrier is that they give a qualitative insight which can help to interpret the quantitative results from the previous section and from the blade load records analysed later.

For example, following the sequence shown in Figs. 16 and 17, we see the beginning of leading edge separation at about $\theta = 75°$ with the separation fully developed by $\theta = 110°$. This corresponds very well to the lift break shown by the blade load records in Chart VIII. The blade then passes into what can only be called very disturbed flow. Over this region, it is interesting to observe the effect of blade angular velocity as shown by the differences between the sequence in Fig. 16 and that in Fig. 17. Some turbulence is encountered on the return cycle, and the blade seems to be operating at nearly constant negative incidence in the region of $\theta = 272°$, and 308° which also agrees with the load curve in Chart VIII.

At the higher advance ratio (Figs. 19 and 20), there is no obvious separation until $\theta = 145°$, and even then it is not marked. Neither is the turbulence on the return cycle of much strength, after about $\theta = 240°$.

Another flow feature which is of interest is the curvature. The lifting line theory for blade load, which is used in the Appendix and in Ref. 3, stipulates that the downwash be constant over the blade chord, or as expressed in Ref. 3, "that the blade chord should be very small with respect to the smallest radius of curvature of the cycloid". Clearly, the radius of curvature of the flow encountered by the blade is comparable to, or even less than, the blade chord over the region from $\theta = 140°$ to $\theta = 220°$. A load distribution theory which can account for such a curved flow must be used to predict the blade forces over this region.

Chart I - Blade Flow Parameters for Idealised Inflow

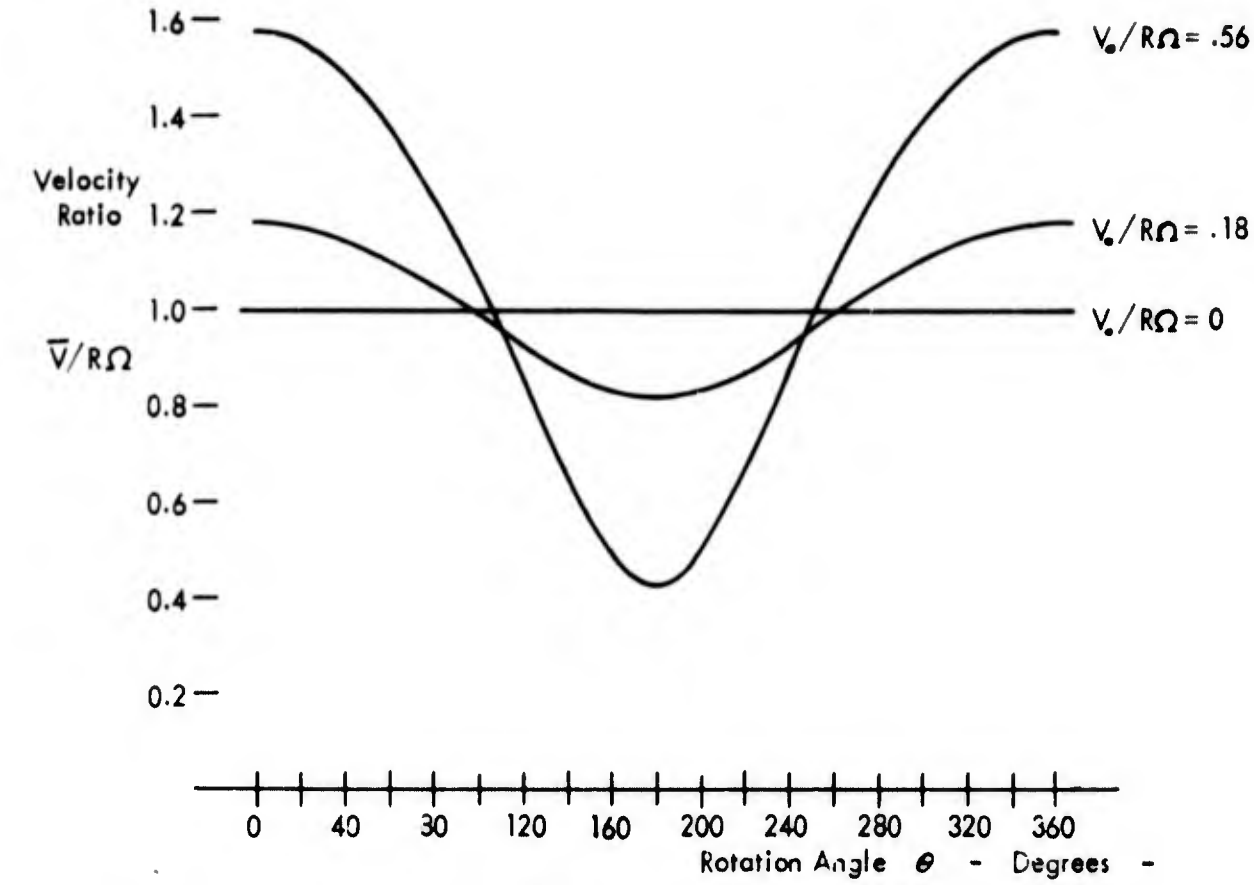

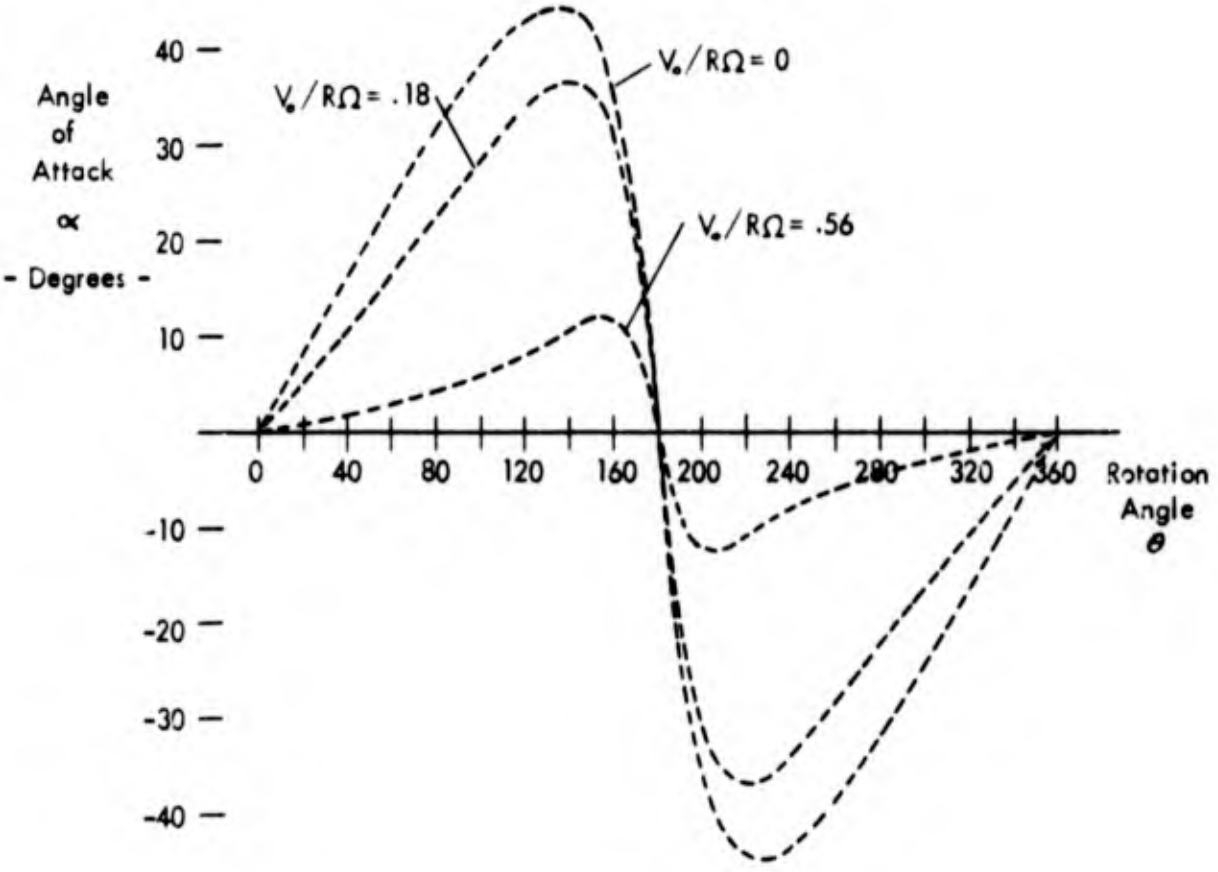

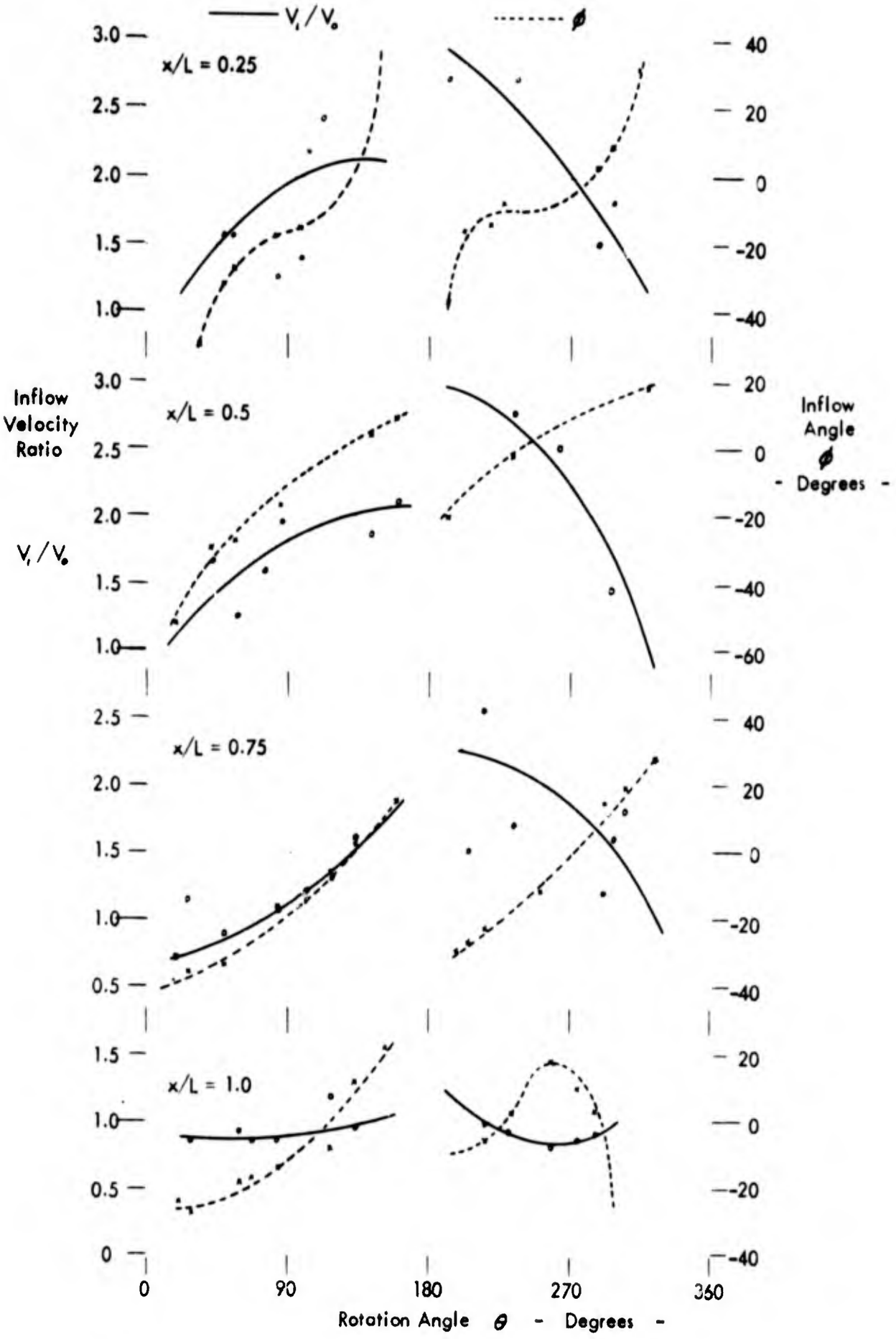

Chart II - Measured Inflow Properties at $V/\pi ND = .18$

Chart III - Blade Flow Parameters at $V/\pi ND = .18$

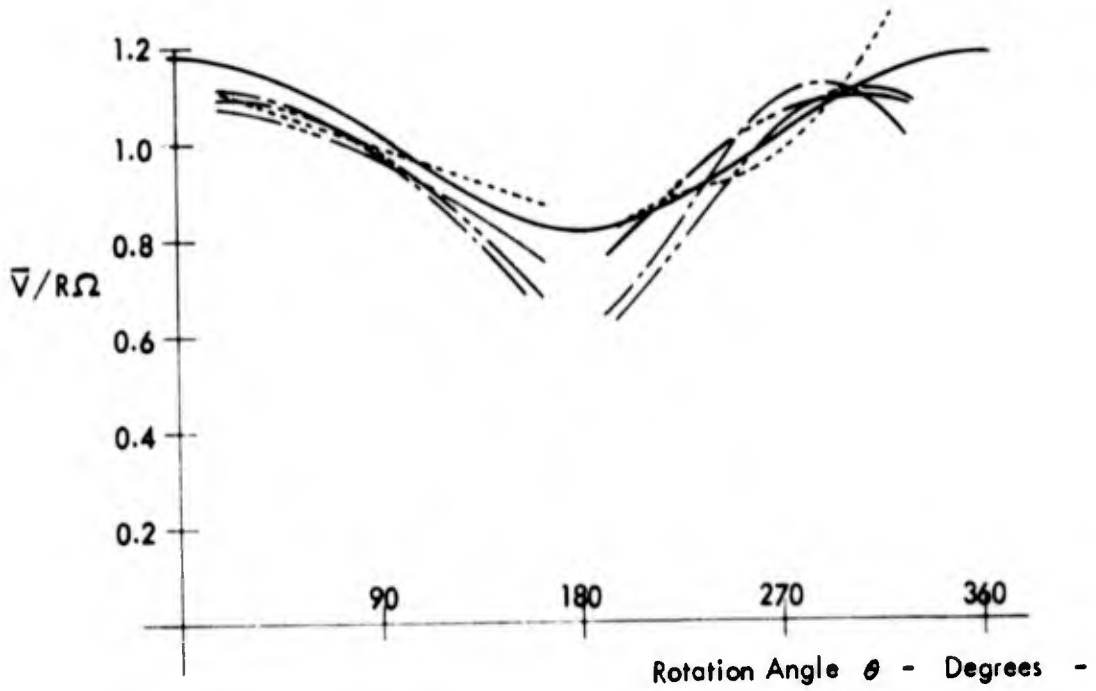

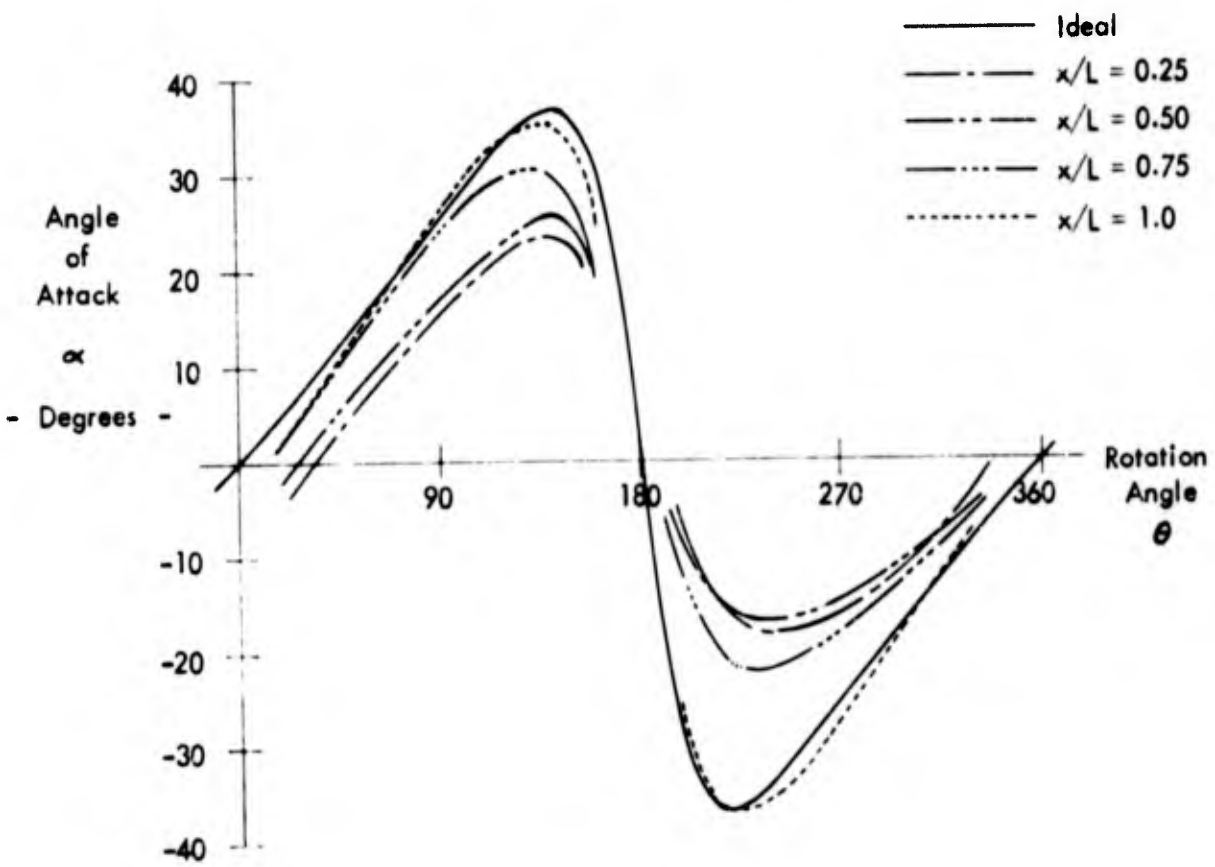

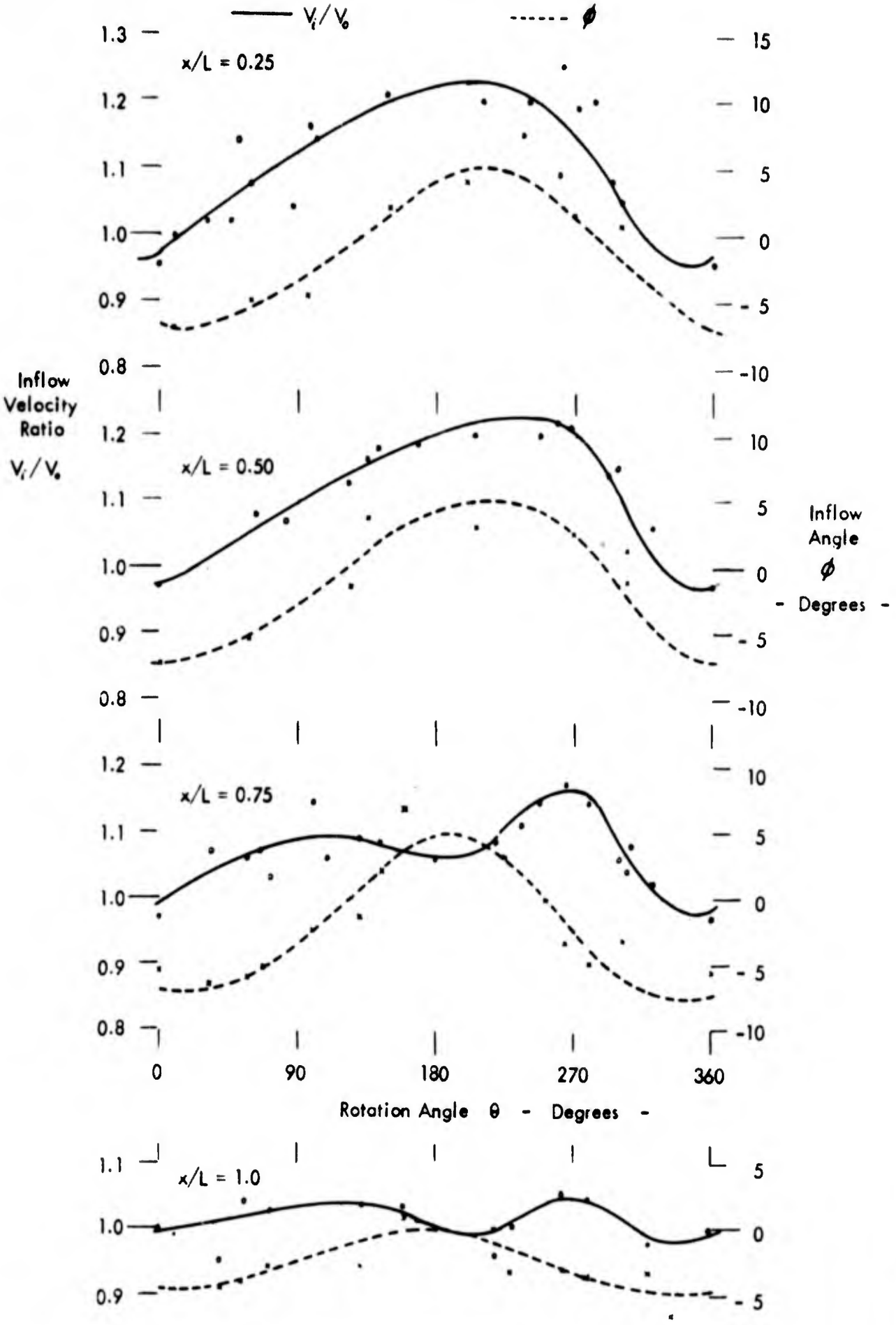

Chart IV - Measured Inflow Properties at V/πND = .575

Chart V - Blade Flow Parameters at $V/\pi ND = .575$

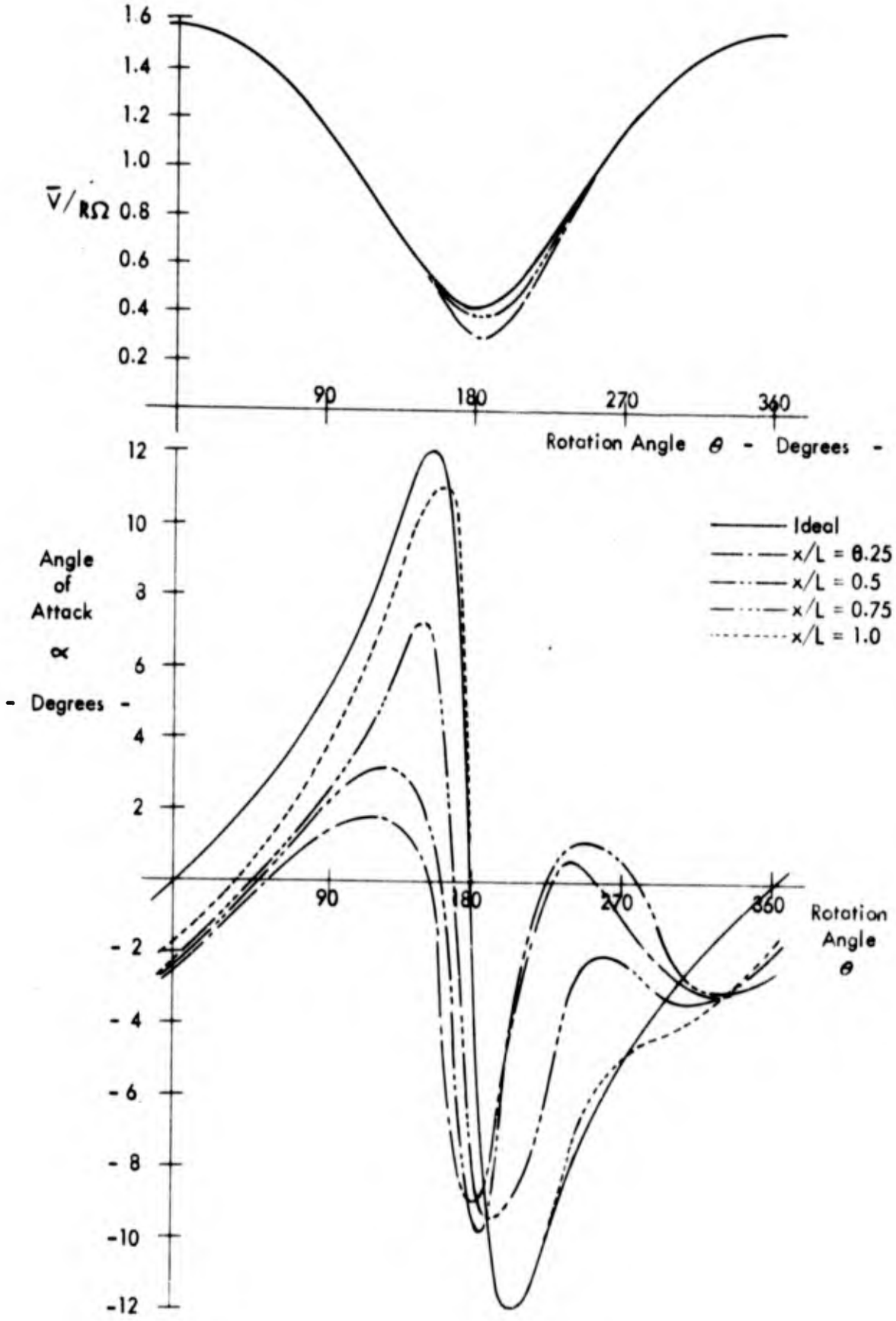

Chart VI - Blade Load and Thrust Curves at $V/\pi ND = .575$

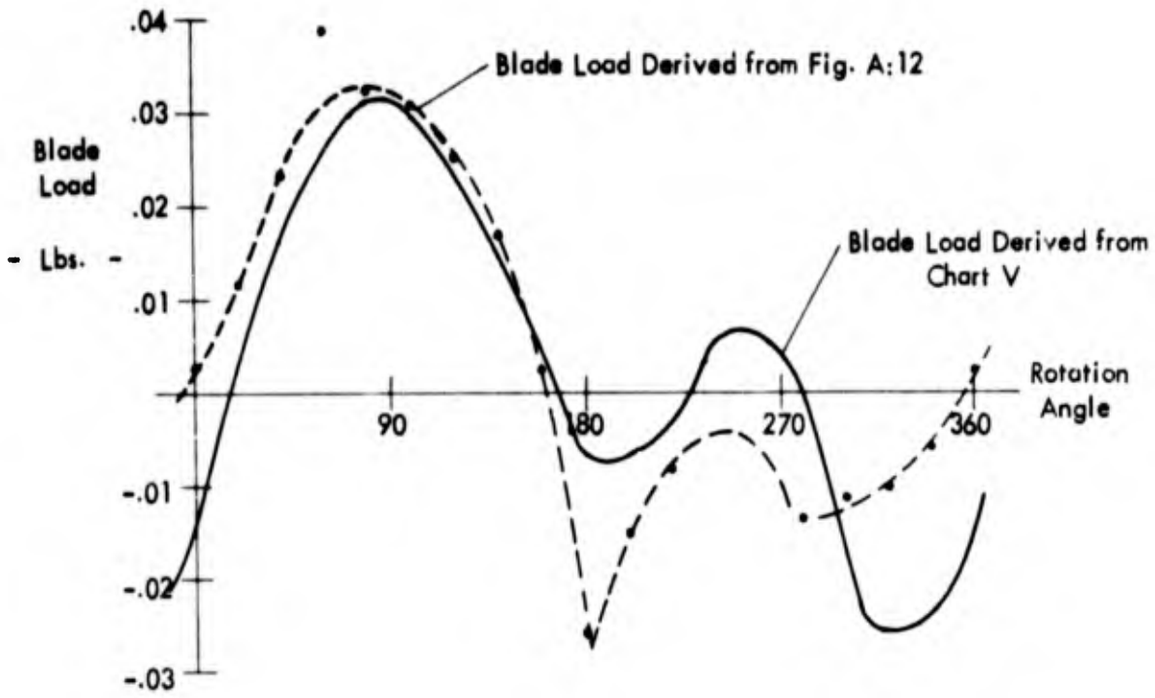

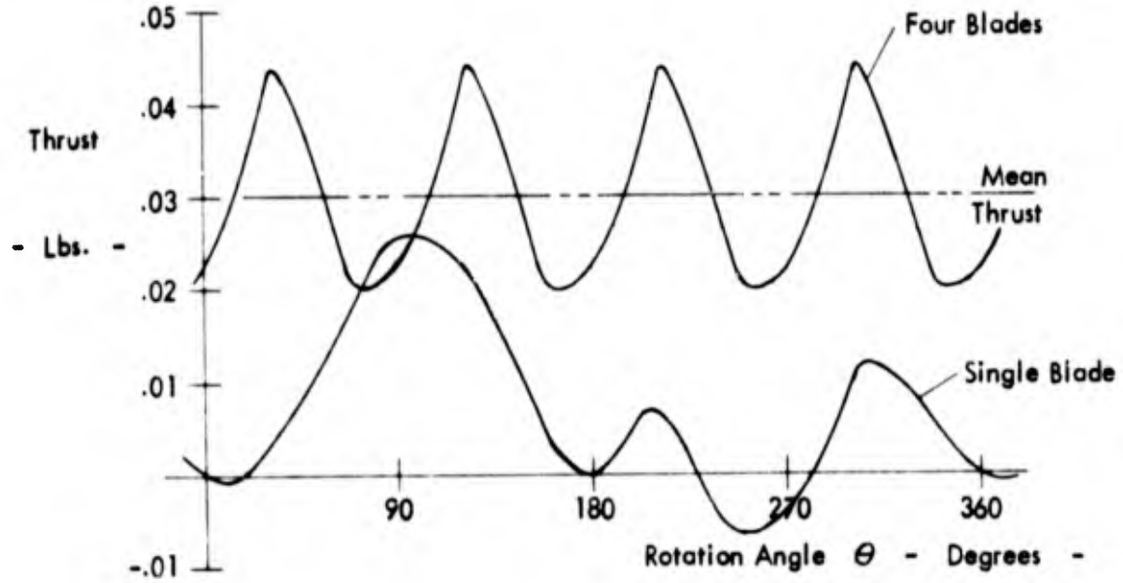

Chart VII - Comparison of Inflow Results - J = 1.8

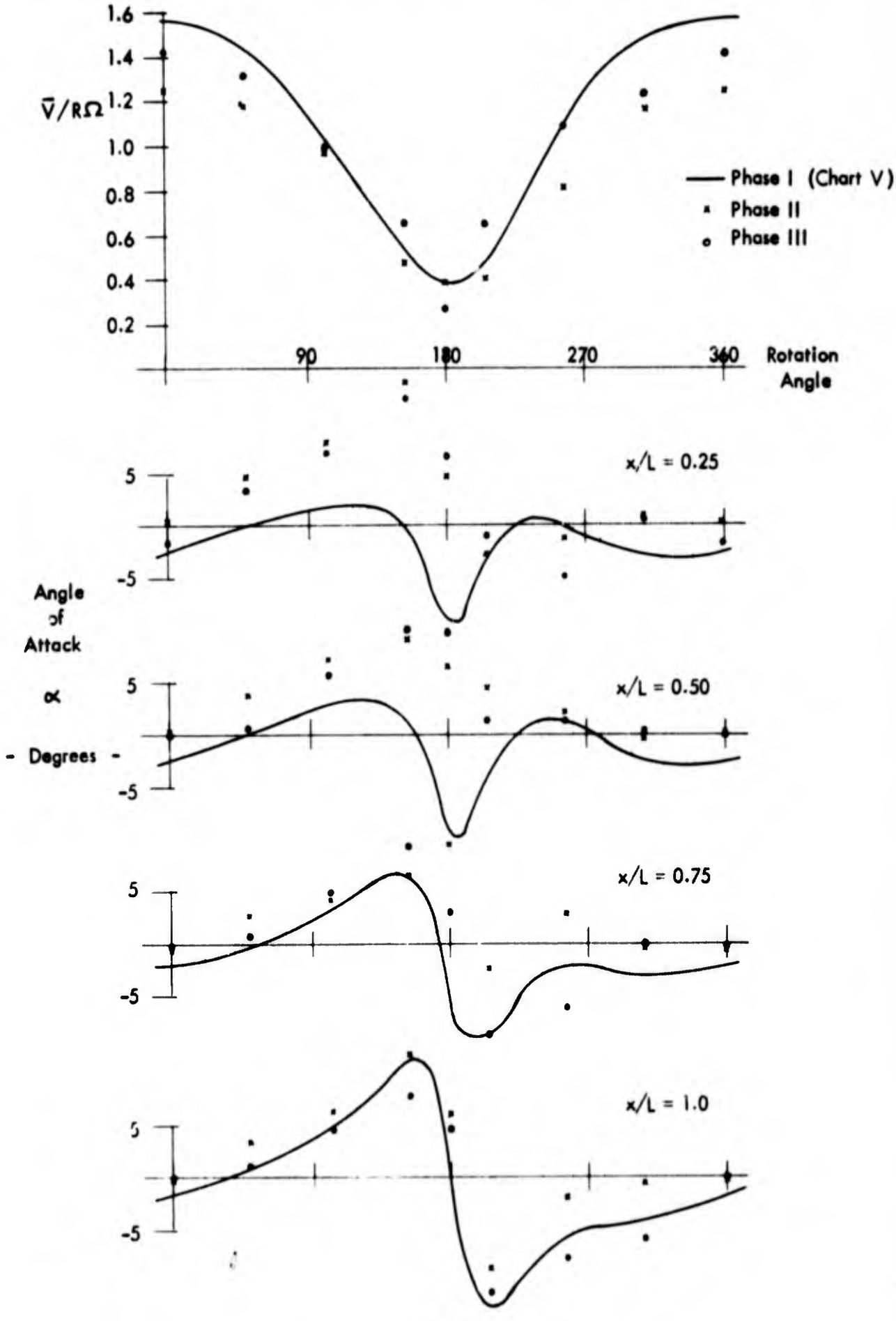

5.3 Analysis of Blade Load Records

The direct measurement of blade force, was complicated by the appearance of a very high level of vibration in the natural mode of the blade on its spring mount. As there was no sign of mechanical excitation of this mode when the unit was operated in air (Fig. A:4), then excitation of this mode must be of hydrodynamic origin. However, the source of the excitation remains obscure. If it were due to some form of stall flutter, one would expect it to be high at the low advance ratios, disappearing as forward speed is increased. But this does not happen.

Nor is the vibration excited by some form of buffet or encountered turbulence - the vibration level is equally great on the upstream part of the cycle when the inflow is regular. Whatever the source of excitation, it is quite strong, as the normal mode of the blade, when at rest, is very heavily damped.

The blade load time histories, corrected for the gravity and centrifugal effects, are given in Chart VIII. In the upper portion, we have the loads for the low advance ratio, $J = .556$, for both the two and three dimensional flow cases. In the lower portion, we have the loads for $J = 1.8$, once again for the two and three dimensional flow conditions. The differences due to the end plate (making the flow two dimensional) are quite interesting.

At the low advance ratio, addition of the endplate maintains the lift of the blade to a higher incidence, probably due to the suppression of the tip vortex. On the other hand, suppression of the large spanwise flow component (see Figs 11 and 12) over the return portion of the cycle, appears to reduce the

lift of the blade over this region to a considerable degree.

The situation at J = 1.8 is reversed. Now it is the three dimensional case which has the greater lift over the forward cycle and the lesser lift over the return.

The final step is to calculate the thrust due to the blade load, and these results are shown in Chart IX, both the individual blade thrust and the total thrust.

At low advance ratio (J = .556) the thrust of the three dimensional configuration is some 20% greater than that of the two dimensional, due to the extra blade lift developed on the return cycle. The thrust variation is also less for the three dimensional case; $\pm$ 23% as against 28%.

At J = 1.8, the thrust of the three dimensional configuration is 10% lower than that of the two dimensional arrangement. The thrust variation is $\pm$ 23% in both cases. The reason for this, as for the higher blade load shown in Chart VIII, is probably that the section lift slope is much higher in the two dimensional case, as shown in the Appendix.

In Chart X, the thrust coefficient calculated from the figures above are compared with the results given in Ref. 4. The figures obtained by the flow visualisation methods are consistently low. It must be remembered that the loads measured or deduced in this program are all very low and there is a strong possibility that the percentage error is high. The Reynolds Number of the test is also very low; could have the effect of reducing the lift slope of the blade over the whole cycle and will certainly reduce the blade lift over the region of high blade incidence. Then too, the results given in Ref. 4, although for a very similar

propeller configuration, do not necessarily have the steering centre exactly at the right angles to the flow, but somewhat offset to optimise the thrust. It is encouraging, nevertheless, to see the trend of the results of this program in general agreement with those of Ref. 4.

Chart VIII - Measured Blade Load Time Histories

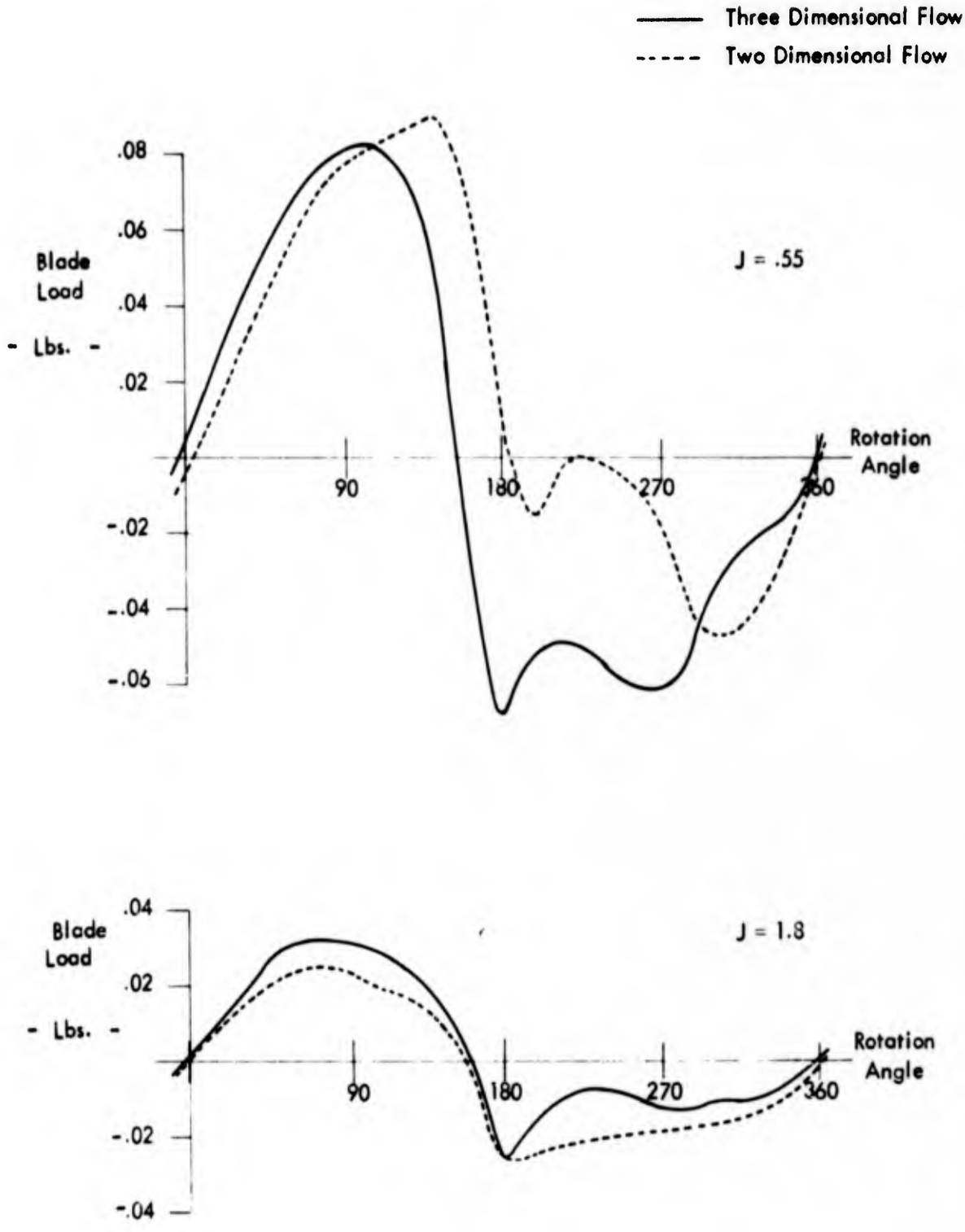

Chart IX - Thrust Time Histories deduced from Measured Blade Loads

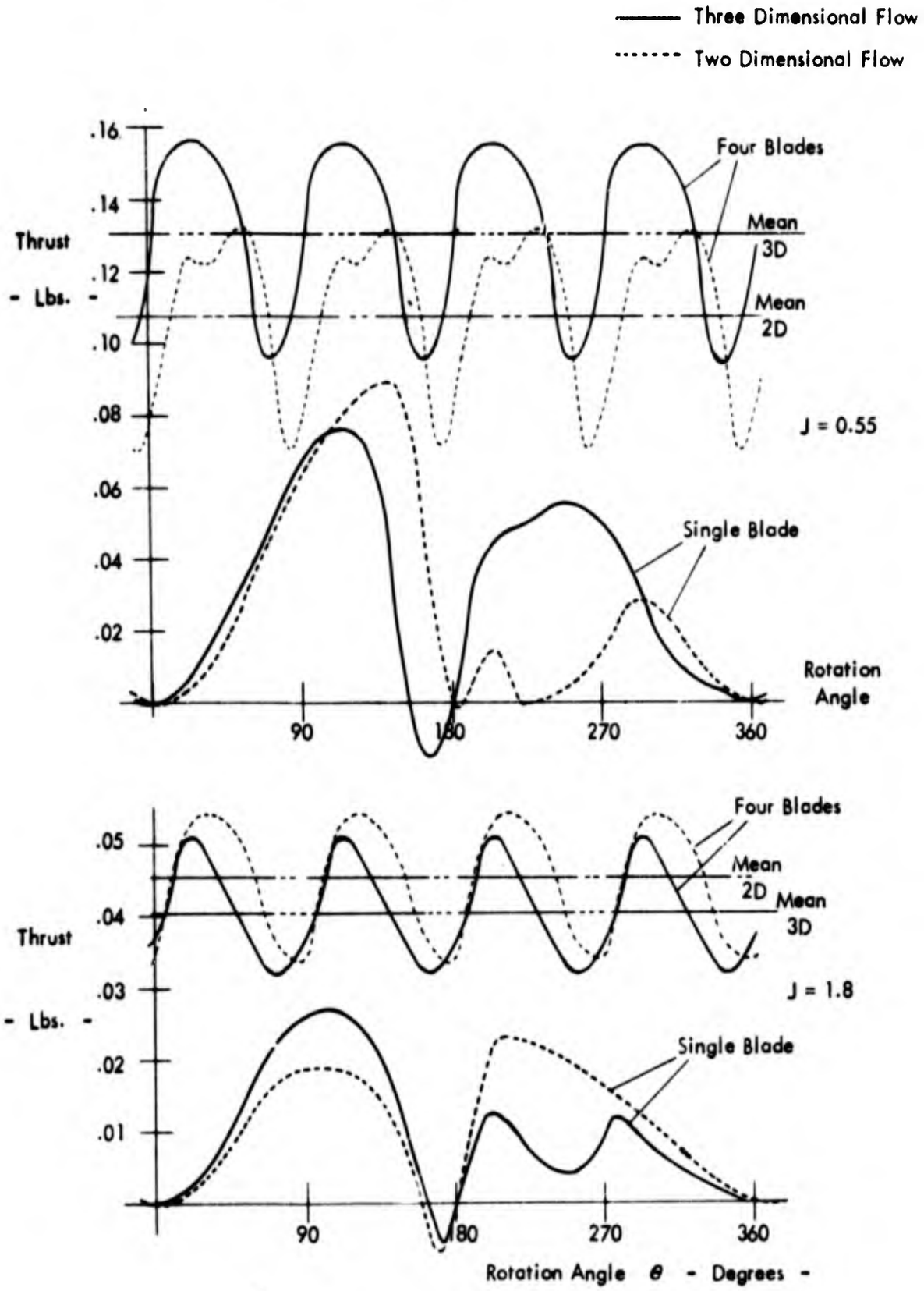

Chart X - Comparison of Thrust Coefficients

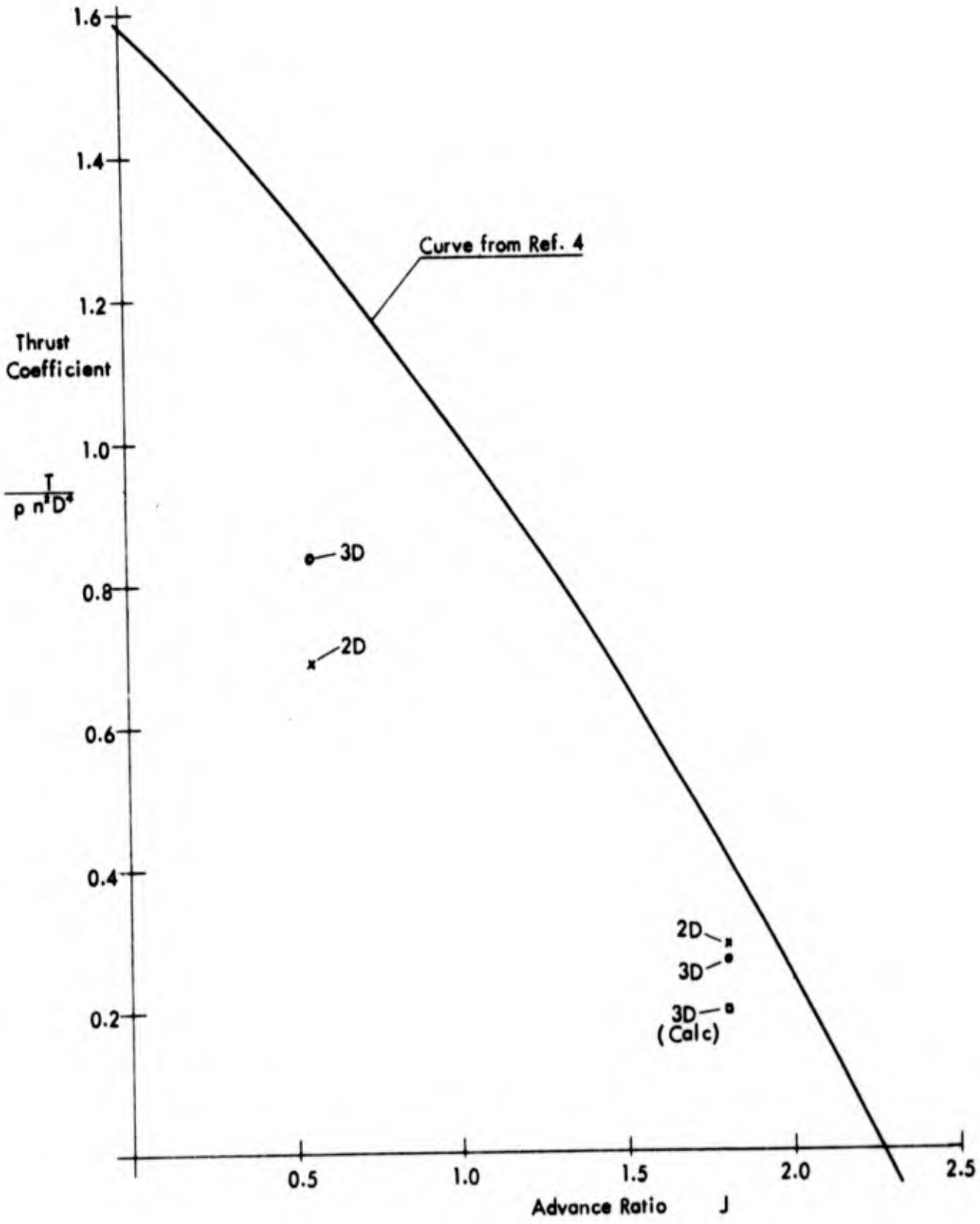

6.0 CONCLUSIONS

This program was primarily intended to explore and demonstrate the application of flow visualisation techniques to the study of cycloidal propeller problems. The results have amply demonstrated that useful data, both qualitative and quantitative, can be derived through the use of the present methods. In addition, some useful engineering guides to design have been found.

1) If the propeller is designed to operate at low advance ratio (as in a tug) and it is desirable to instal a guard to prevent blade damage from influx of debris, such a guard should be an open mesh type permitting spanwise flow. A closed type of guard will result in loss of performance.

2) If the propeller is to operate at high speed, a closed guard will increase performance by raising the lift effectiveness of the blades.

3) There is plenty of scope for development of blade motion mechanisms which will derive more lift over the return cycle.

For development of the flow visualisation technique into a routine experimental tool for cycloidal propeller studies the following suggestions seem justified:

1) Effort should be concentrated on the use of the general flow photograph technique. This is by far the simplest to make, requires the minimum model and permits a higher, much more representative Reynolds Number. The existing model, for example could be run at about 500 RPM in the NRC facility with an advance ratio $J = 1.8$. Some refinement of the photography method would be necessary, for example shutter triggering directly by the rotation of the model.

2) The rotating camera technique, for all that it provides spectacular film for direct viewing, and is useful in giving qualitative insight into the flow characteristics, would require excessive development to yield comparable quantitative data to those given by the general photograph. If further development is to be pursued, a lightweight camera, taking a negative much larger than the 16 mm movie frame is necessary. An automatic 35 mm camera, triggered in a staggered sequence, could probably be operated in the existing assembly up to perhaps 300 RPM.

Further experiments, using some of the improved photographic methods outlined above, could include:

1) Study of the flow with the steering centre offset. This could be done simply by rotating the cam on the existing model.

2) Study of blade motions designed to improve the lift on the return cycle over that given by the "ideal" motion used in the present experiment. This would require new cams.

3) Study of the flow through a propeller with a pitch ratio greater than π . This would require a major rework of the present model.

4) Study of the propeller flow with representative hull shape forward and athwart the unit. Provided these were not too extreme, they could be fitted to the present facility. Also useful in such a program would be the study of debris guard configurations.

7.0 REFERENCES

1) De Young, J., and Harper, C.W., "Theoretical Symmetric Span Loading at Subsonic Speeds for Wings Having Arbitrary Plan Form." NACA Report 921, 1948.

2) Abbot, I.H., and von Doenhoff, A.E., "Theory of Wing Sections" Dover Publications, Inc., 1959.

3) Sparenberg, J.A., "On the Efficiency of a Vertical Axis Propeller" Third Symposium on Naval Hydrodynamics, 1960.

4) Netherlands Ship Model Basin, "Research on Vertical Axis Propellers" Contract Nonr 62558-2630, Mod. 2.

APPENDIX

A:1 Derivation of Blade Loading.

The distribution of hydrodynamic load on a blade is calculated using the method given in Ref. 1. This method is based on a lifting line theory, deriving a matrix of influence coefficients to relate the distribution of load to an imposed spanwise distribution of incidence.

The blade planform and spanwise sections are shown in Fig.A:1. The section profiles have a thickness distribution which closely approximates that for the NACA 65A series of profiles (Ref. 2). The mean line corresponds to the NACA mean line for $a = 0.6$, factored to give a design lift coefficient of 0.25. The angle of zero lift is therefore $\alpha = -1.62°$. The thickness/chord ratio for the blade section reduces from 24% at the root to 5.5% at the tip. Experimental results given in Ref. 2 show the lift curve slope of a similar section to be about 6.20/rad and to be insensitive to thickness/chord ratio.

To find the spanwise load distribution for the blade, following the method of Ref. 1, we have:

$$\alpha_\nu = \sum_{n=1}^{4} a_{\nu n} G_n \qquad \text{for } \nu = 1, 2, 3, 4 \qquad \text{where ...}$$

α_ν is the local angle of attack at wing station ν

G_n is the load coefficient $c\, c_l / 2b$ at station n

$a_{\nu n}$ are the planform influence coefficients relating loading to downwash.

c is the local chord

c_l is the local section lift coefficient, and

b is the span.

The influence coefficients $a_{\nu n}$ are presented in Ref. 1, as functions of the parameter H_ν, defined as follows:

$$H_\nu = \frac{d_\nu\, b}{K_\nu\, c_\nu}$$ where

d_ν is a scale factor, and

K_ν is the ratio of the section lift curve slope to the theoretical value of 2π.

For our blade, we have:

ν	K_ν	c_ν	d_ν	K_ν	H_ν
1	.924	.950	.061	.988	.512
2	.707	1.096	.234	.988	1.704
3	.383	1.317	.381	.988	2.306
4	0	1.575	.320	.988	1.622

from Ref. 1 (pp 21-36) $a_{\nu n} =$

11.205	- 3.223	.085	.187
- 1.762	6.571	- 1.848	.051
.0427	- 1.474	5.165	- 1.345
- .1633	.0893	- 2.597	4.613

To calculate the lift in terms of the downwash, we must invert this matrix, thus:

$a^{-1}_{\nu n} =$

.09759	.05271	.02221	.00985
.02879	.18299	.07566	.02120
.00957	.06017	.25174	.07312
.00828	.03220	.14104	.25788

For unit spanwise incidence, the loading is:

G_n/a = .18236, .30864, .39460, .43940

The overall lift coefficient C_{L_α} is 4.125/rad, and the spanwise centre of pressure is at η_{cp} = .4278

For the two dimensional, or endplated case, we assume that the section lift coefficient of 6.20/rad is maintained and becomes the overall lift coefficient C_{L_α}. The span loading is shown below for comparison with that calculated above. The spanwise centre of pressure in this case is at η_{cp} = .455.

A:2 Calibration of Blade Strain Gage.

The strain gaged blade was calibrated by measuring the deflection due to loading at four spanwise stations. The slopes of these four load-deflection curves are then plotted to show the recorder sensitivity in terms of spanwise loading point.

The sensitivities for the two centres of pressure defined above are:

for η_{cp} = .4278, $d\delta/dP$ = .4090 units/gm., or 185.4 units/lb.

for η_{cp} = .455, $d\delta/dP$ = .447 units/gm., or 202.7 units/lb.

Figure A:1 - Blade Planform and Profile Distribution

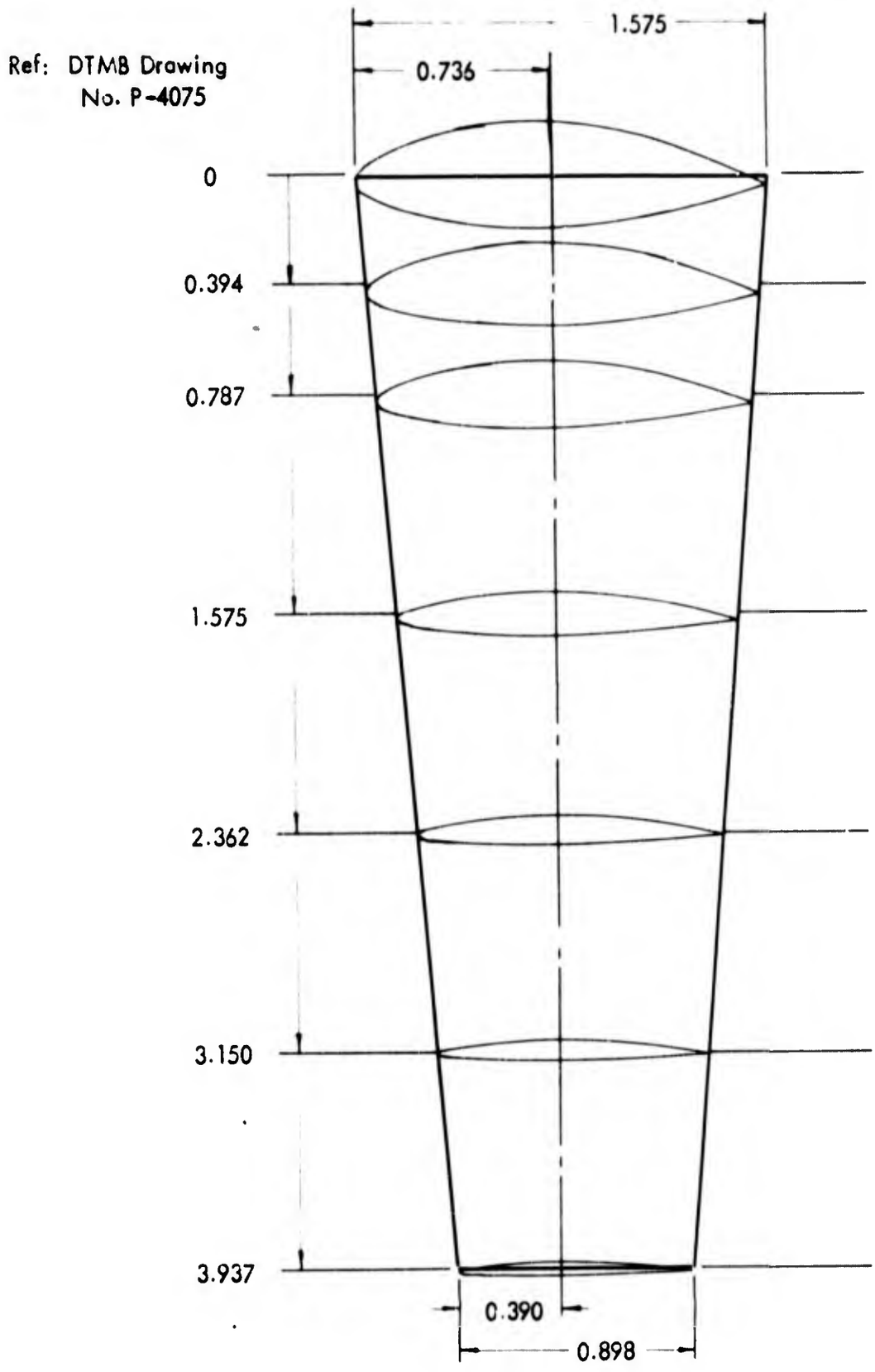

Figure A:2 - Blade Span Load Distribution

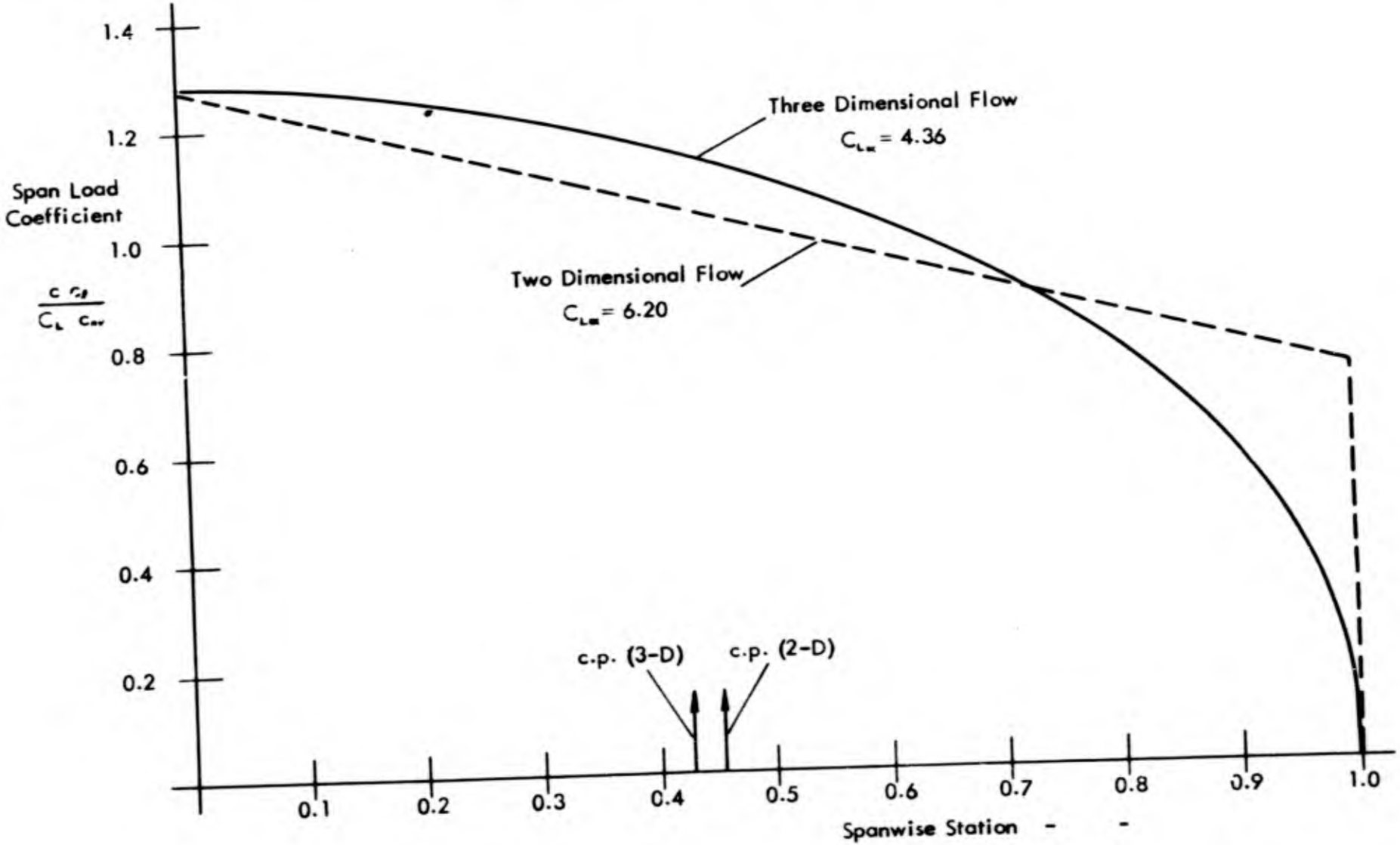

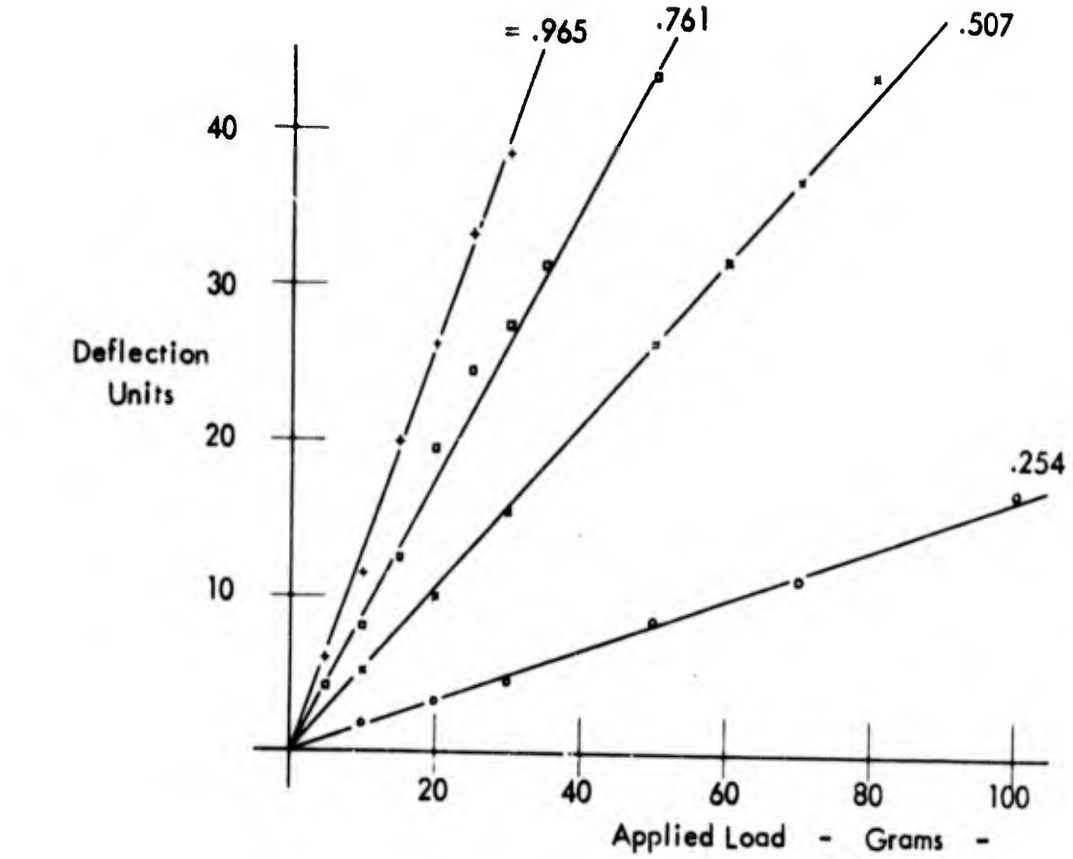
= .965
.761
.507
.254
40
30
20
10
Deflection
Units
20
40
60
80
100
Applied Load - Grams -

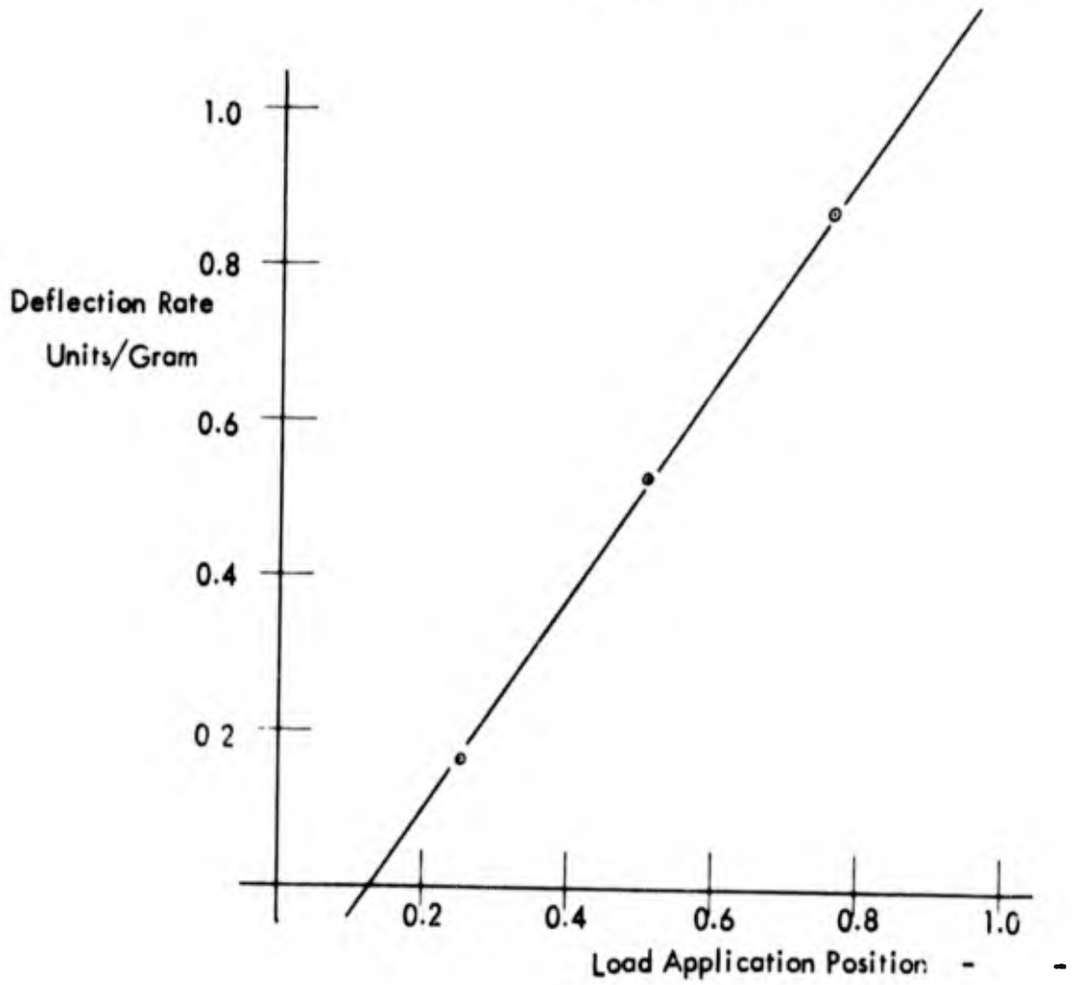
1.0
0.8
0.6
0.4
0 2
Deflection Rate
Units/Gram
0.2
0.4
0.6
0.8
1.0
Load Application Position - -

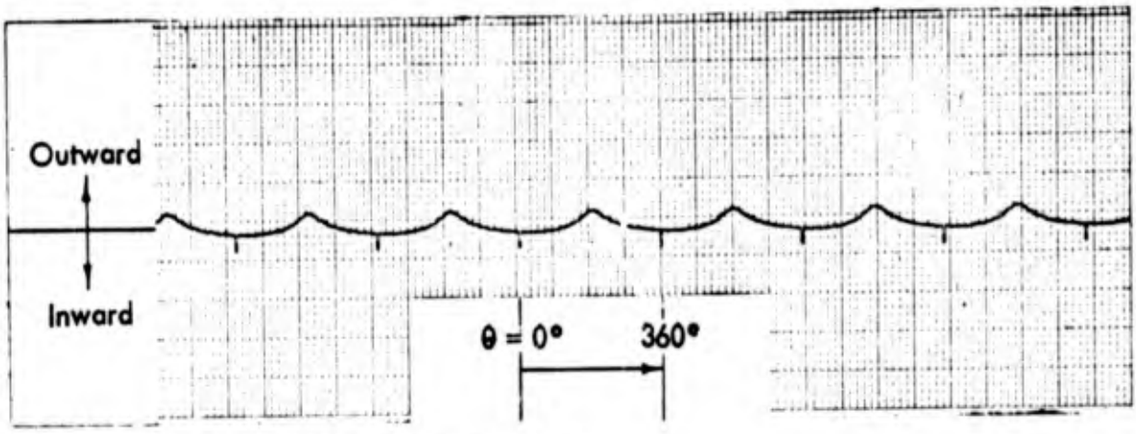

Figure A:4 - Trace with model in air

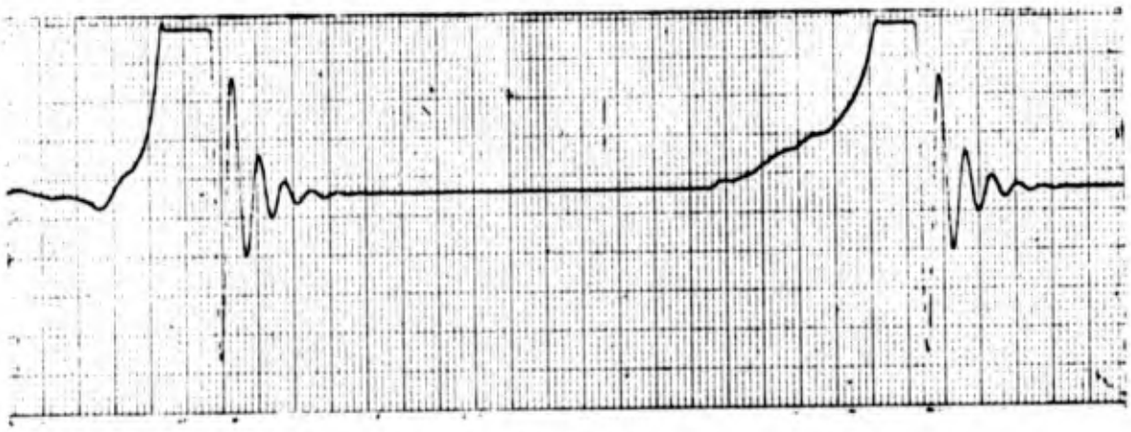

Figure A:5 - Blade natural mode on spring

Natural Frequency = 28.0 cps.

Damping Coefficient γ = .1104/.66 = .1675

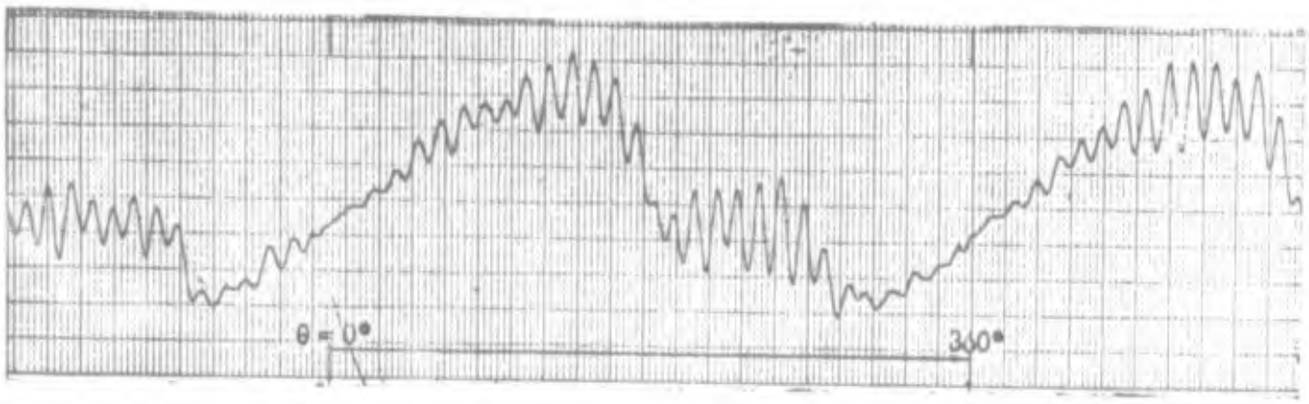

Figure A:6 - Blade Load - Two Dimensional Flow - J = 0.5

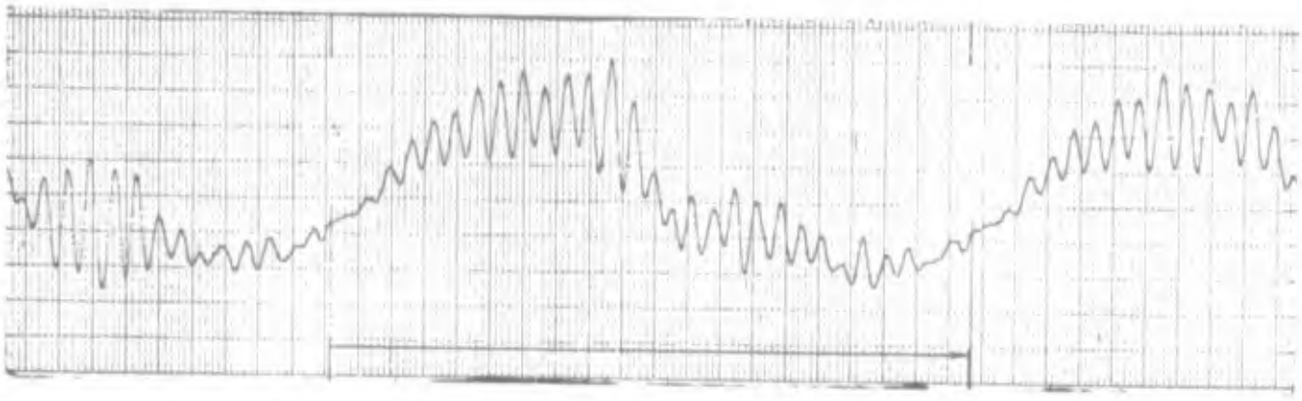

Figure A:7 - Blade Load - Two Dimensional Flow - J = 1.25

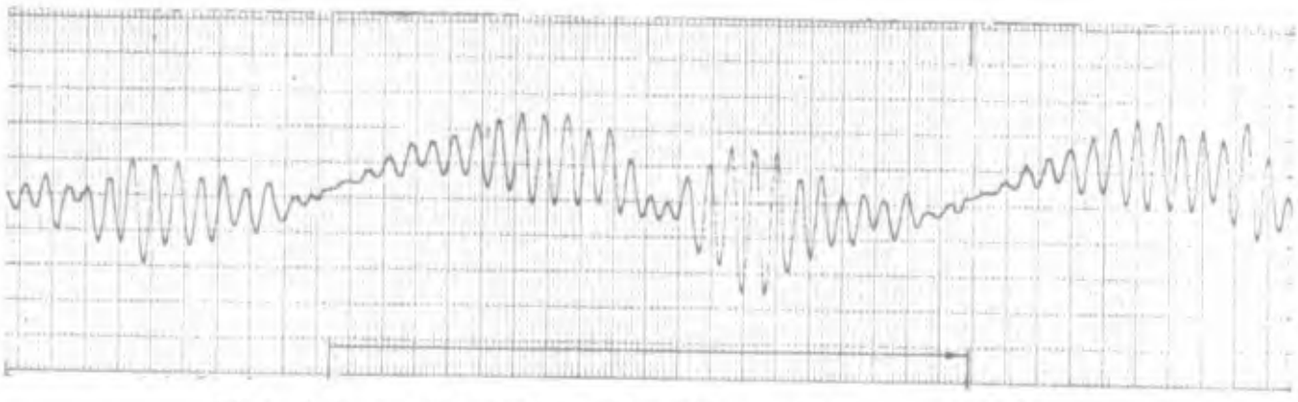

Figure A:8 - Blade Load - Two Dimensional Flow - J = 1.75

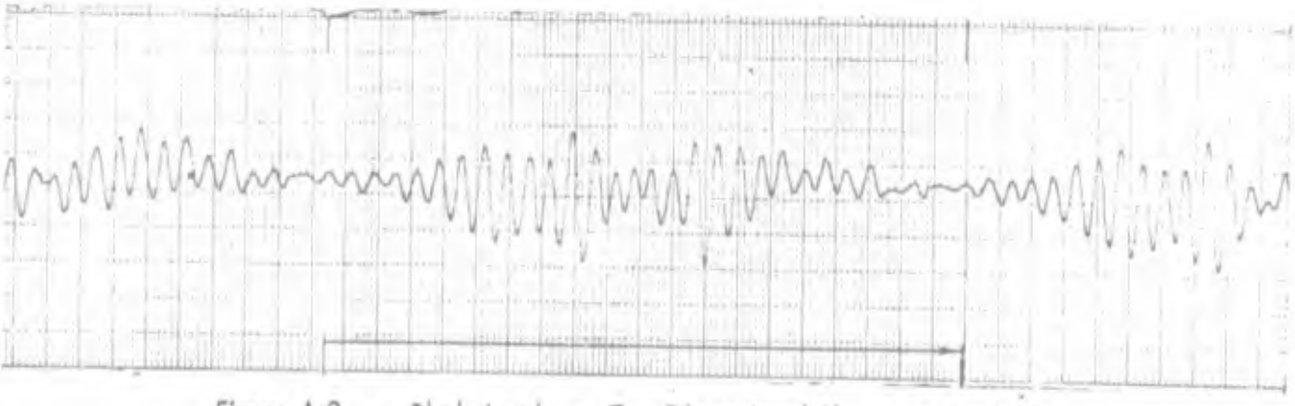

Figure A:9 - Blade Load - Two Dimensional Flow - J = 2.25

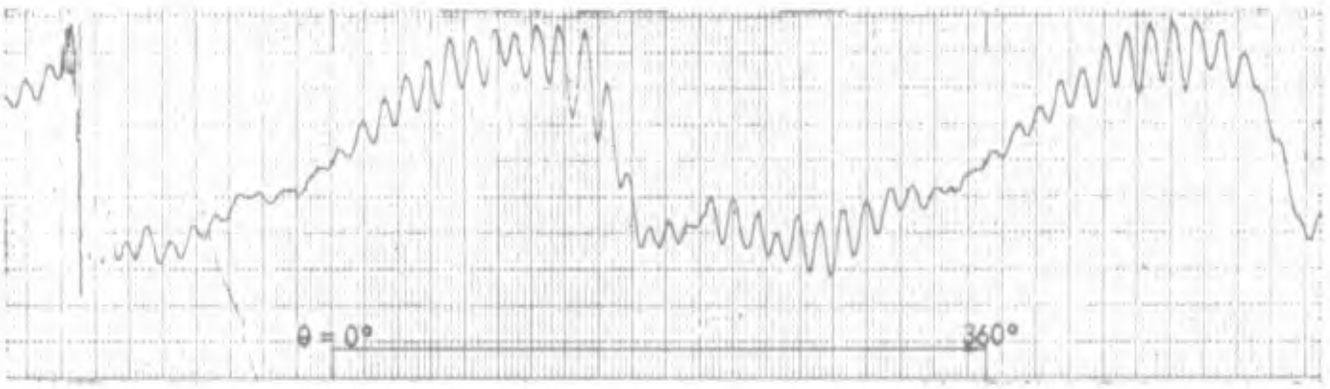

Figure A:10 - Blade Load - Three Dimensional Flow - J = 0.5

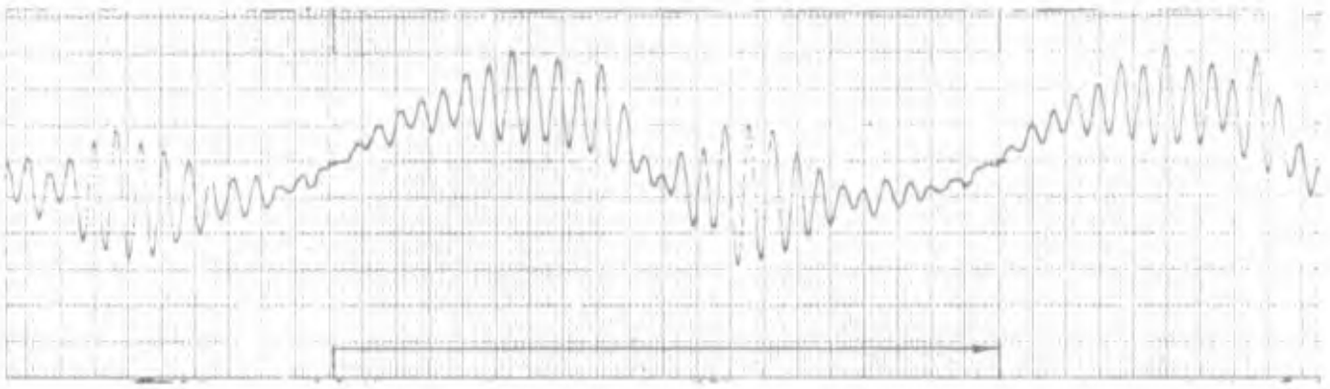

Figure A:11 - Blade Load - Three Dimensional Flow - J = 1.25

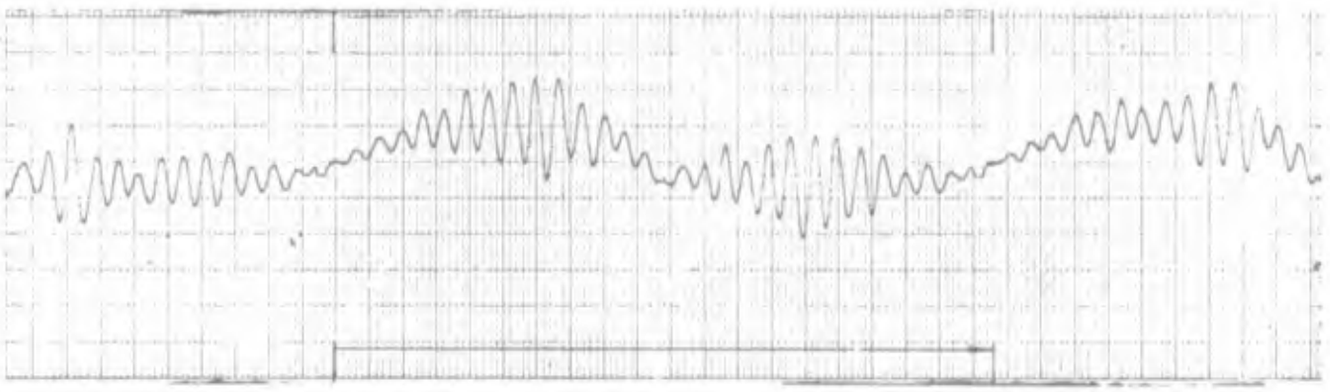

Figure A:12 - Blade Load - Three Dimensional Flow - J = 1.75

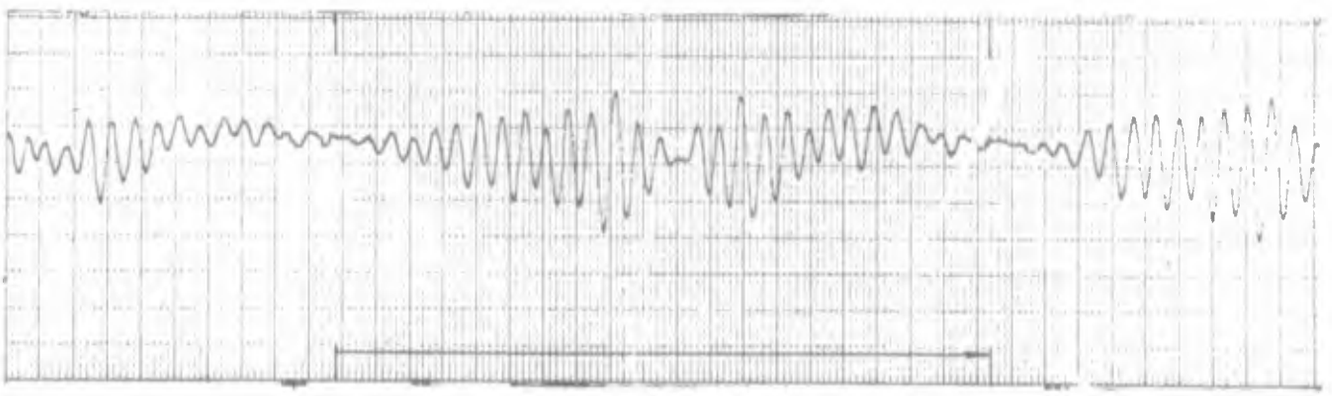

Figure A:13 - Blade Load - Three Dimensional Flow - J = 2.25

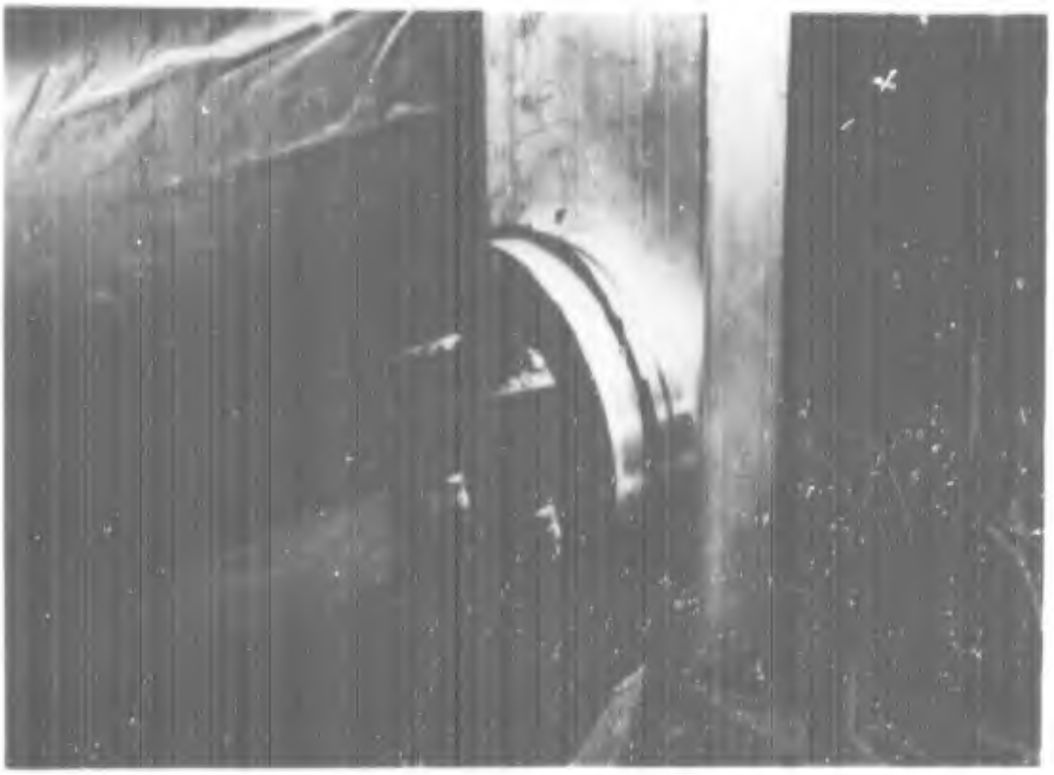

Figure 1 - General View of Model

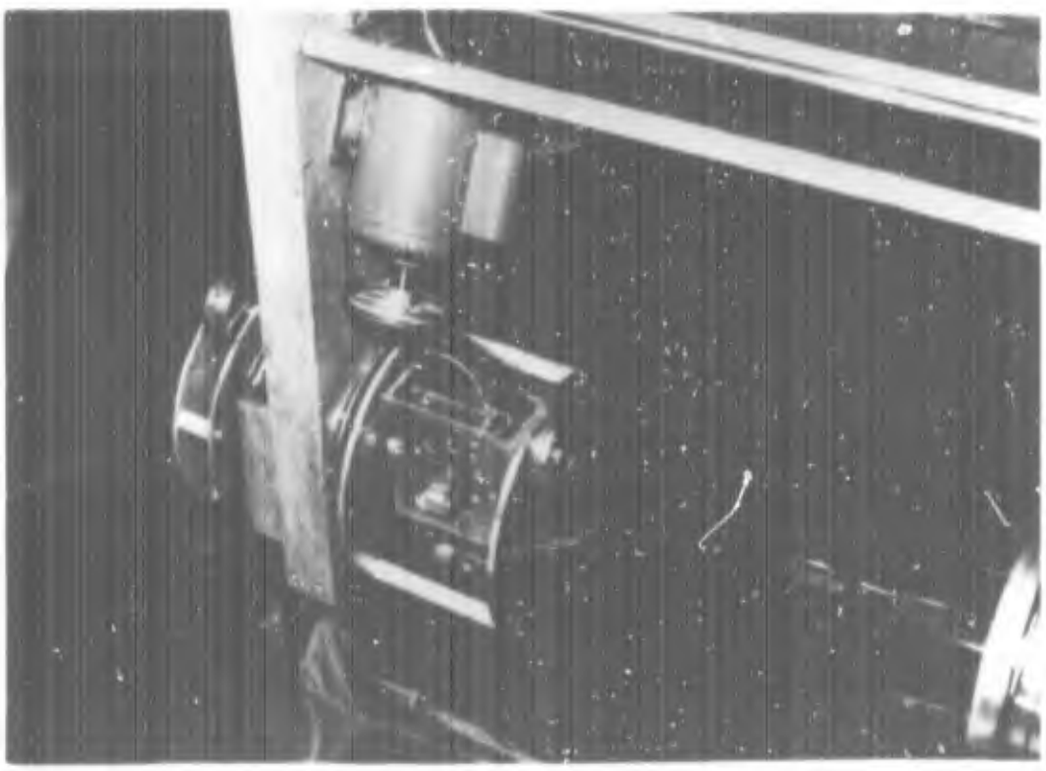

Figure 2 - General View of Camera Carrier

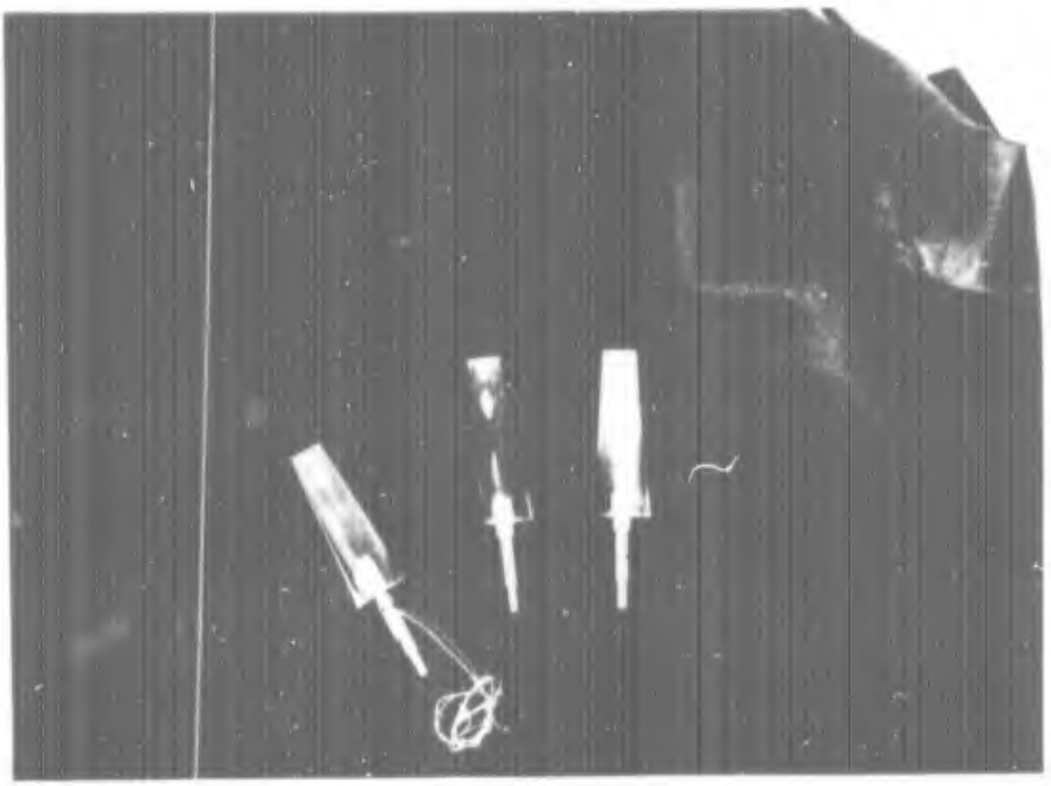

Figure 3 - Blades for Test Model

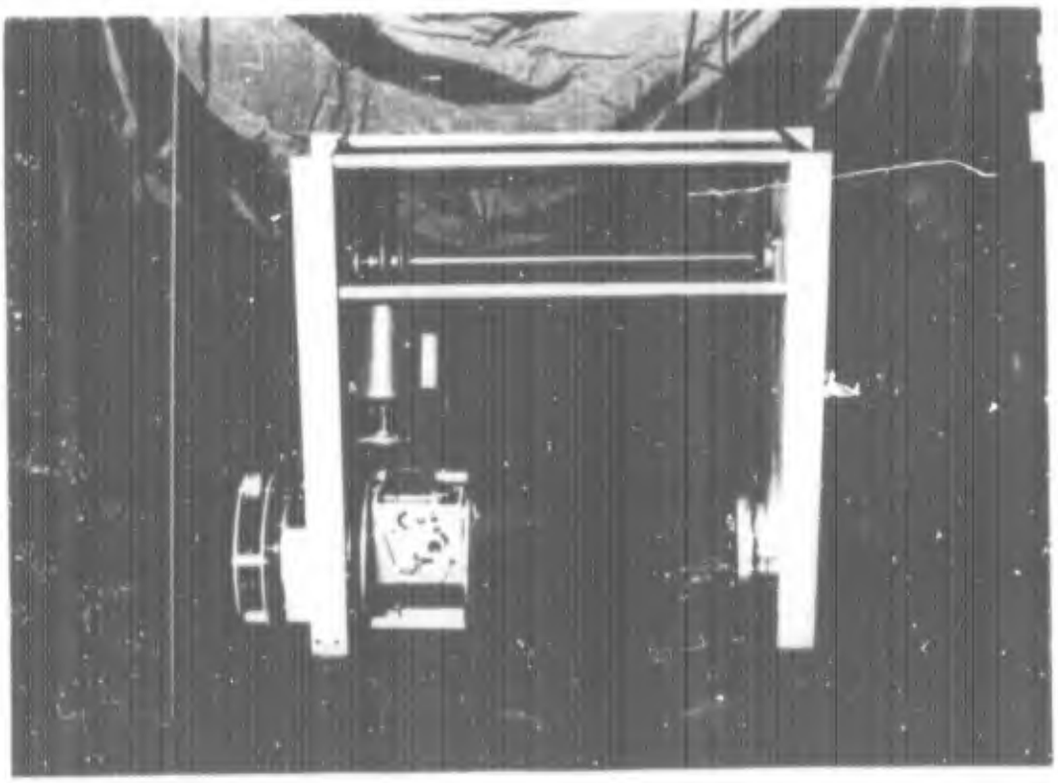

Figure 4 - Assembled Model and Camera Carrier

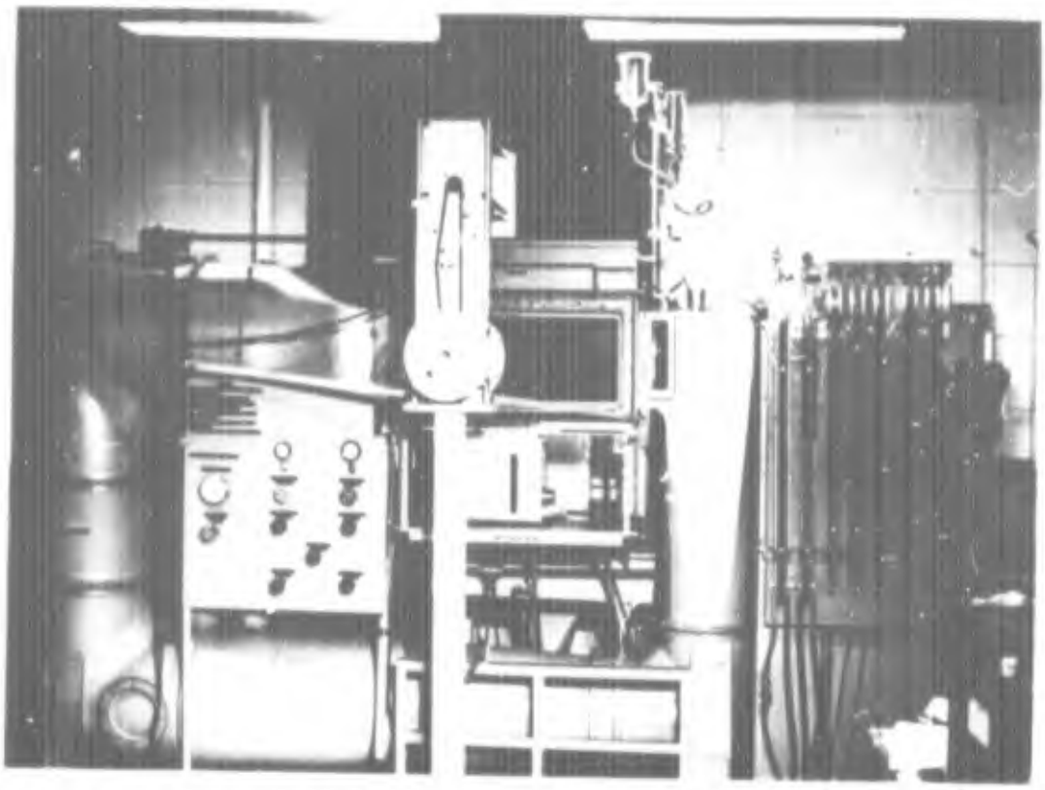

Figure 5 - General View of Water Tunnel with Model Installed

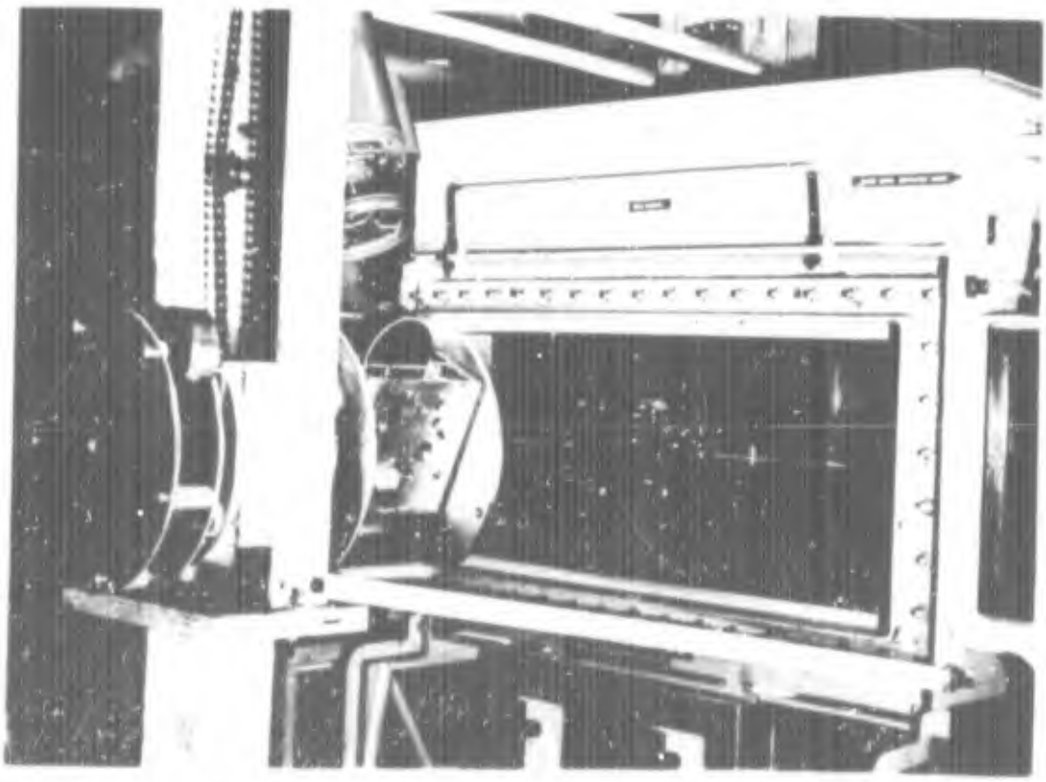

Figure 6 - View of Working Section with Model Installed

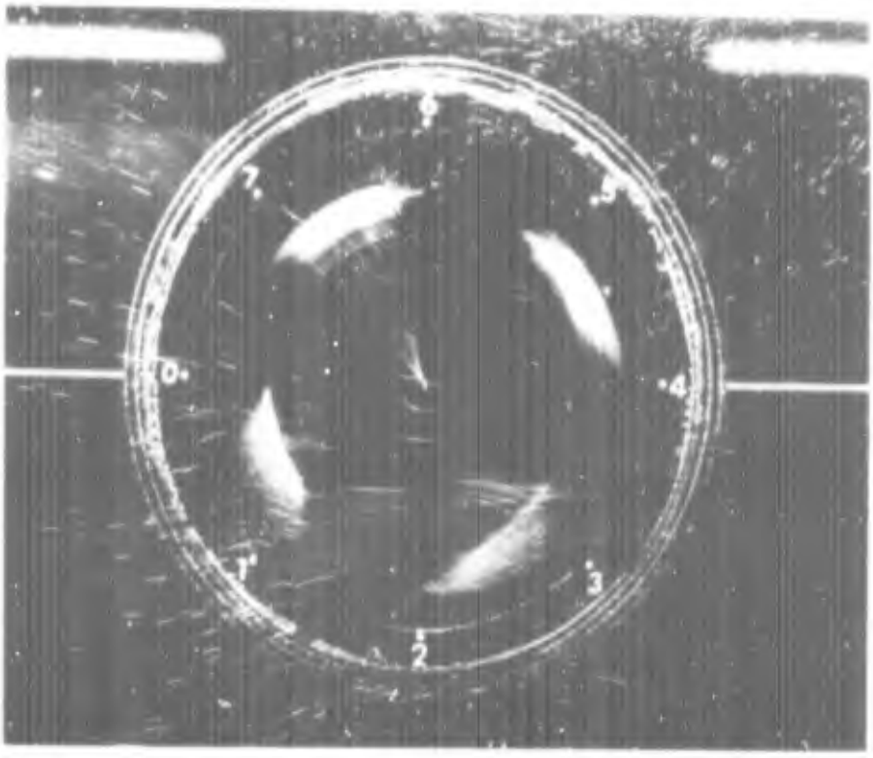

Figure 7 - General Flow Section - V/ND = 0.5 - x/L = 0.5

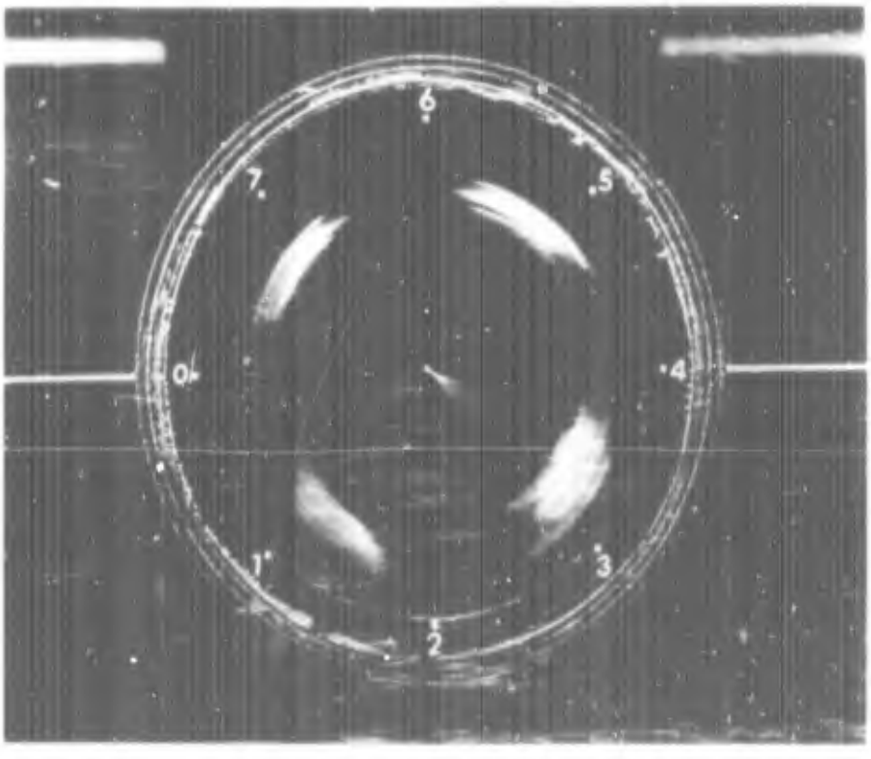

Figure 8 - General Flow Section - V/ND = 1.25 - x/L = 0.5

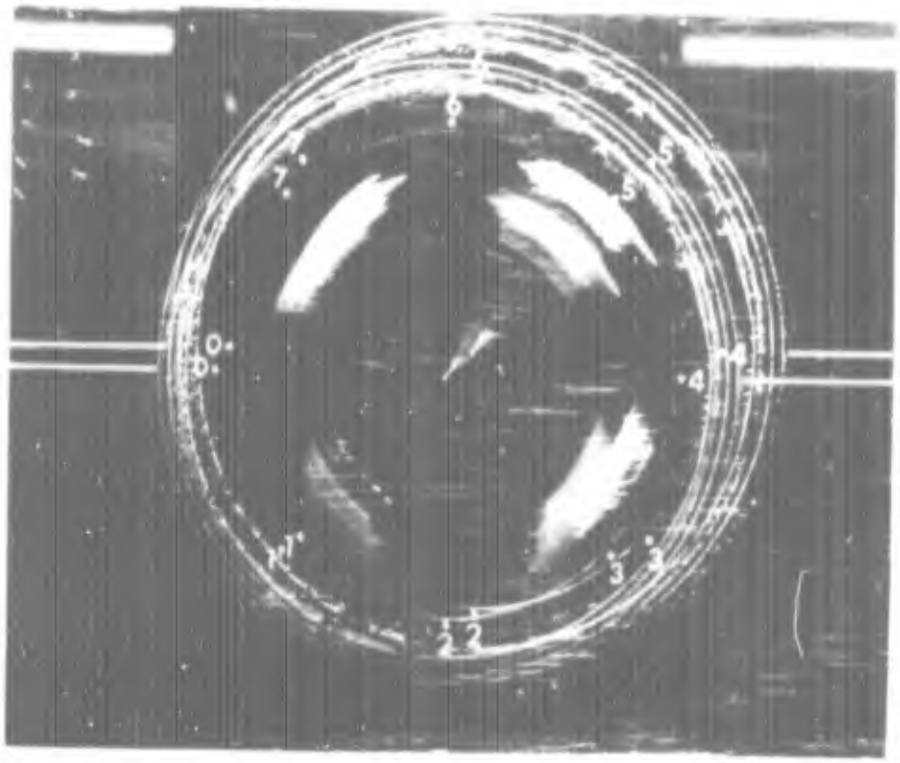

Figure 9 - General Flow Section - V/ND = 1.75 - x/L = 0.5

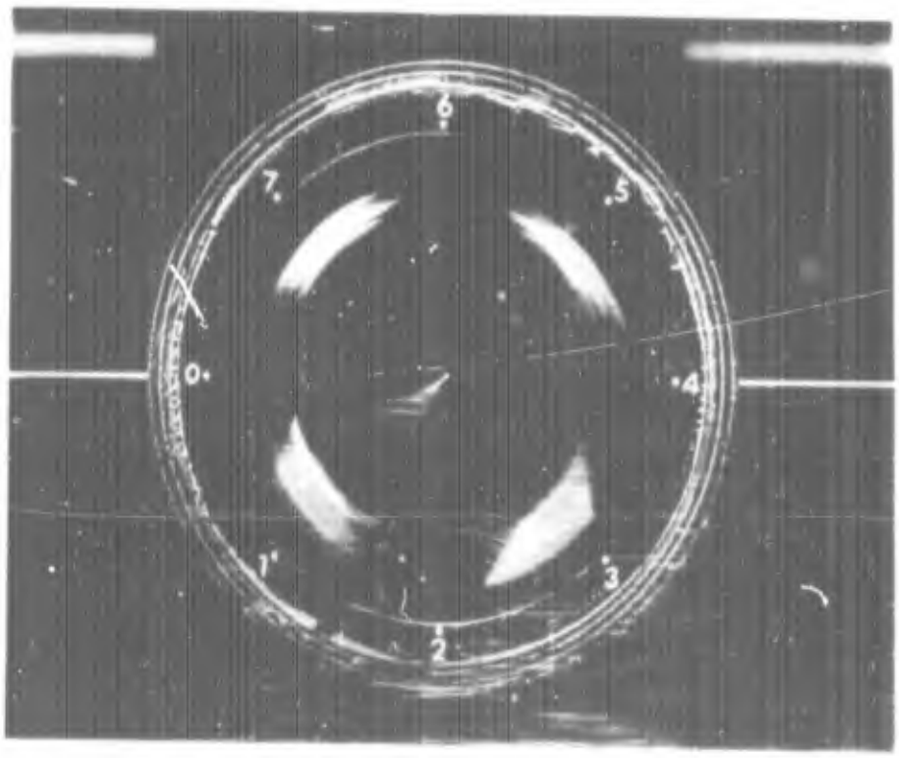

Figure 10 - General Flow Section - V/ND = 2.25 - x/L = 0.5

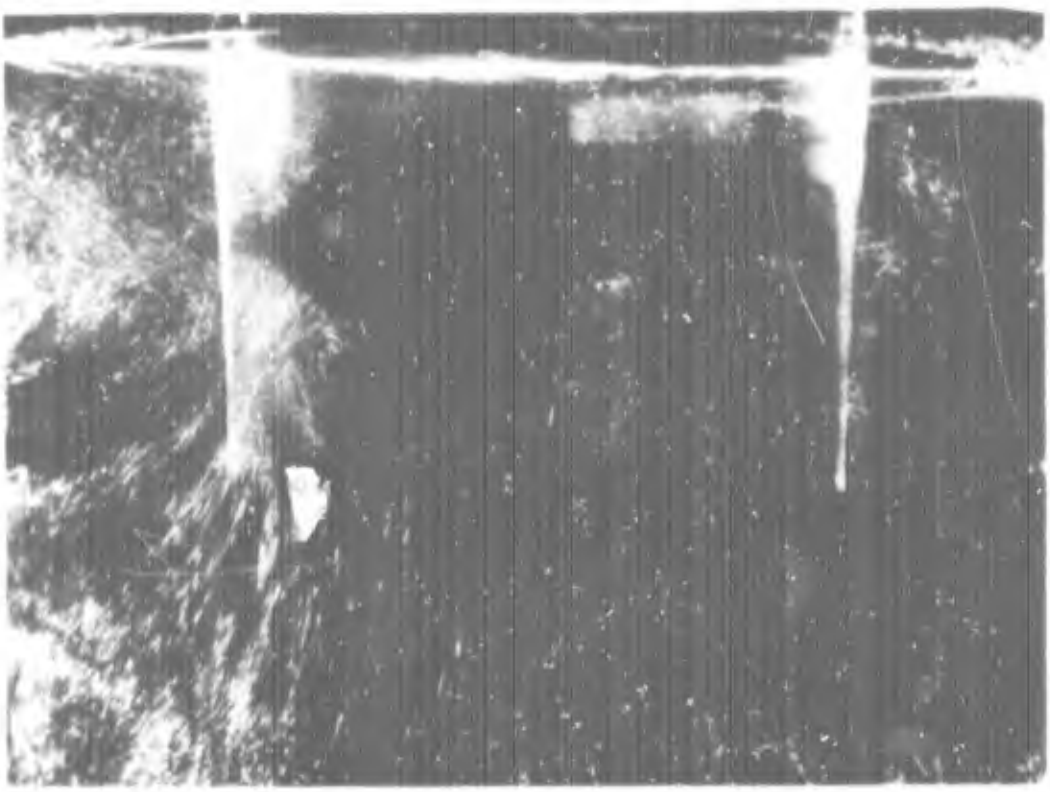

Figure 11 - Transverse Section at Centerline - V/ND = 0.5

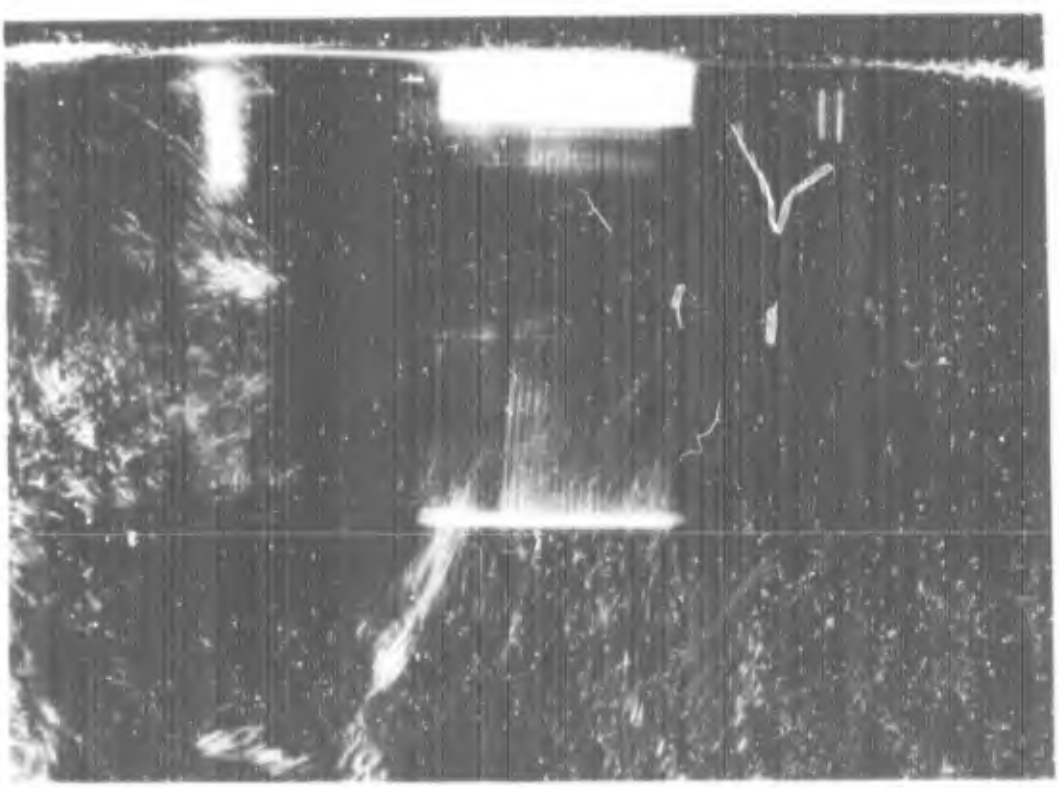

Figure 12 - Transverse Section at Rear Radius - V/ND = 0.5

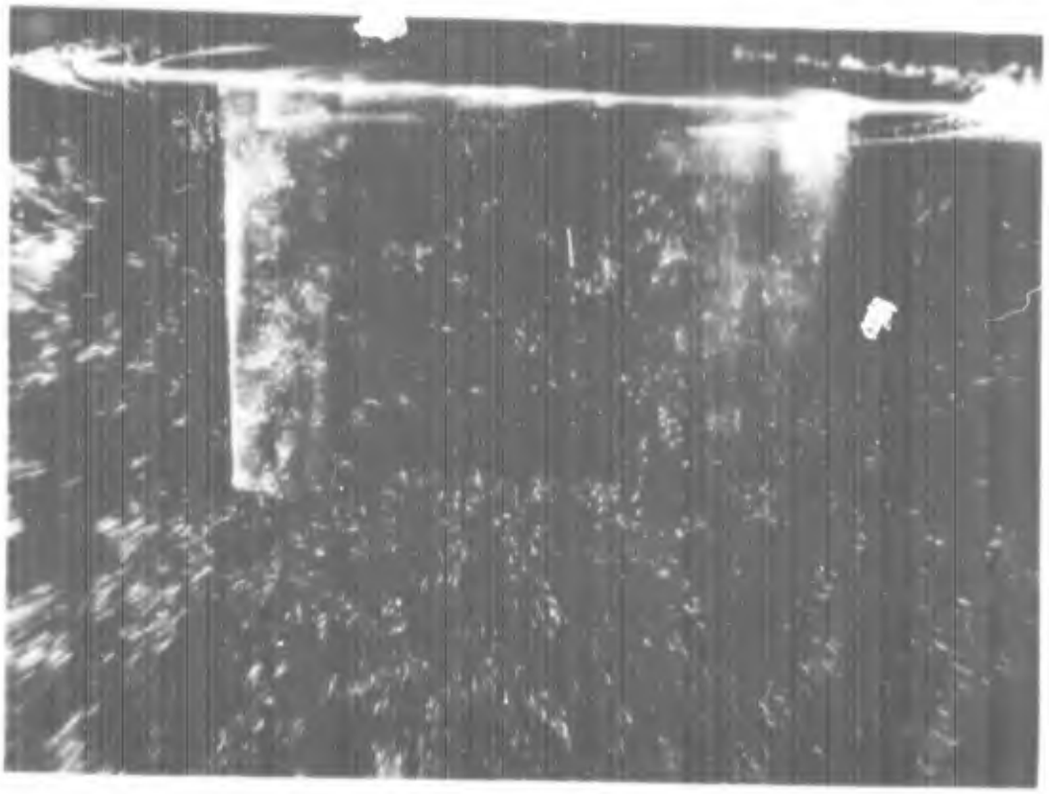

Figure 13 - Transverse Section at Centerline - V/ND = 1.75

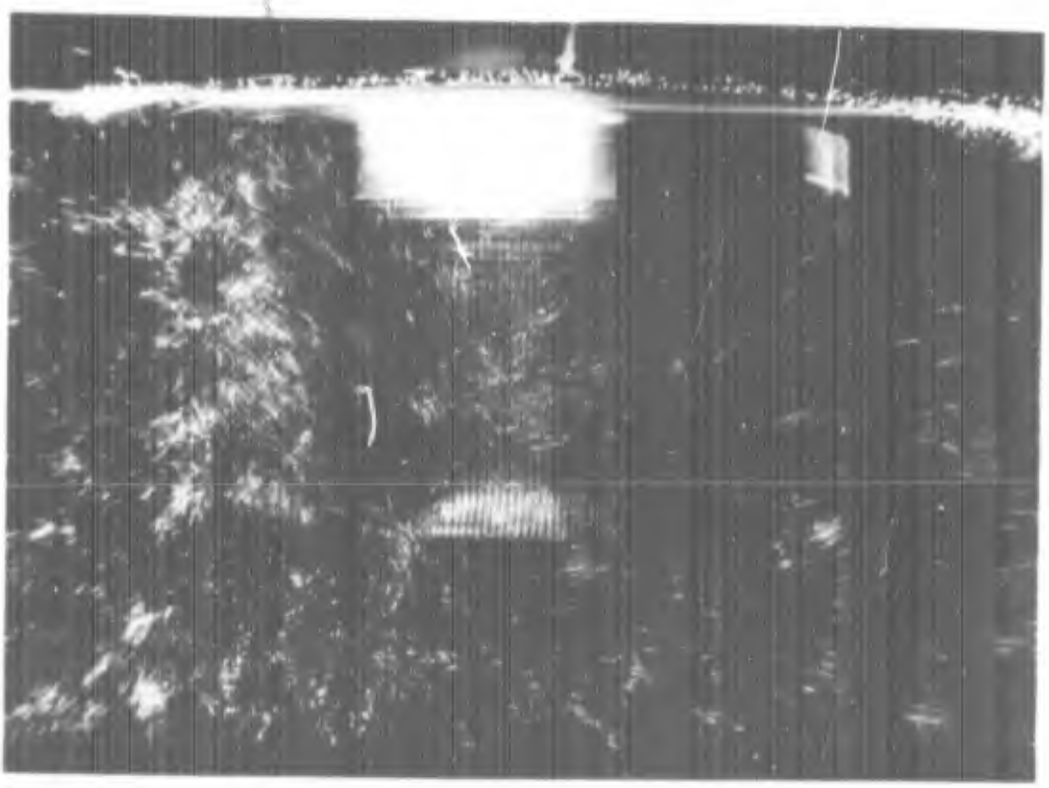

Figure 14 - Transverse Section at Rear Radius - V/ND = 1.75

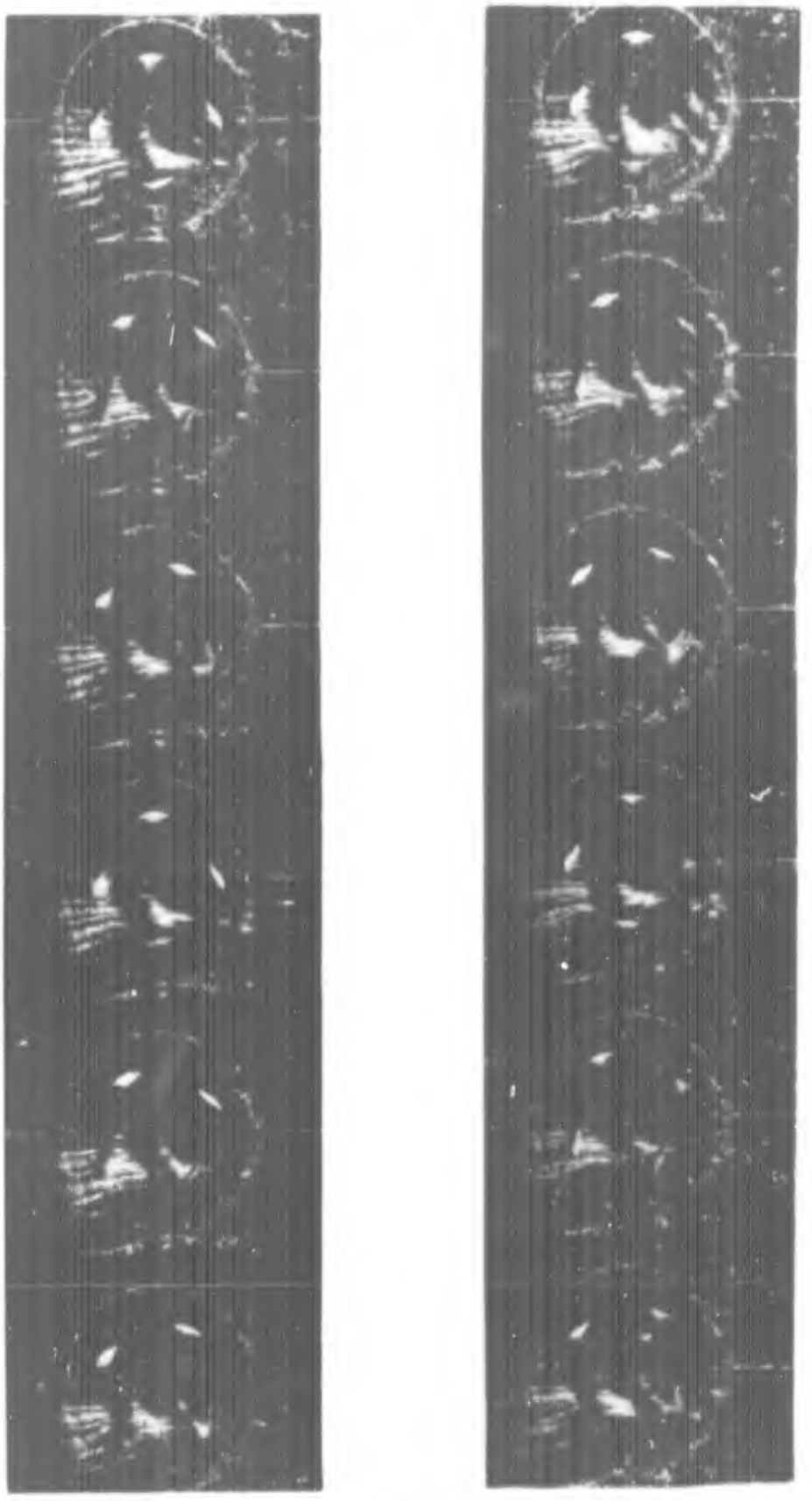

Figure 15 - One Revolution at V/ND = 0.5 - x/L = 0.5

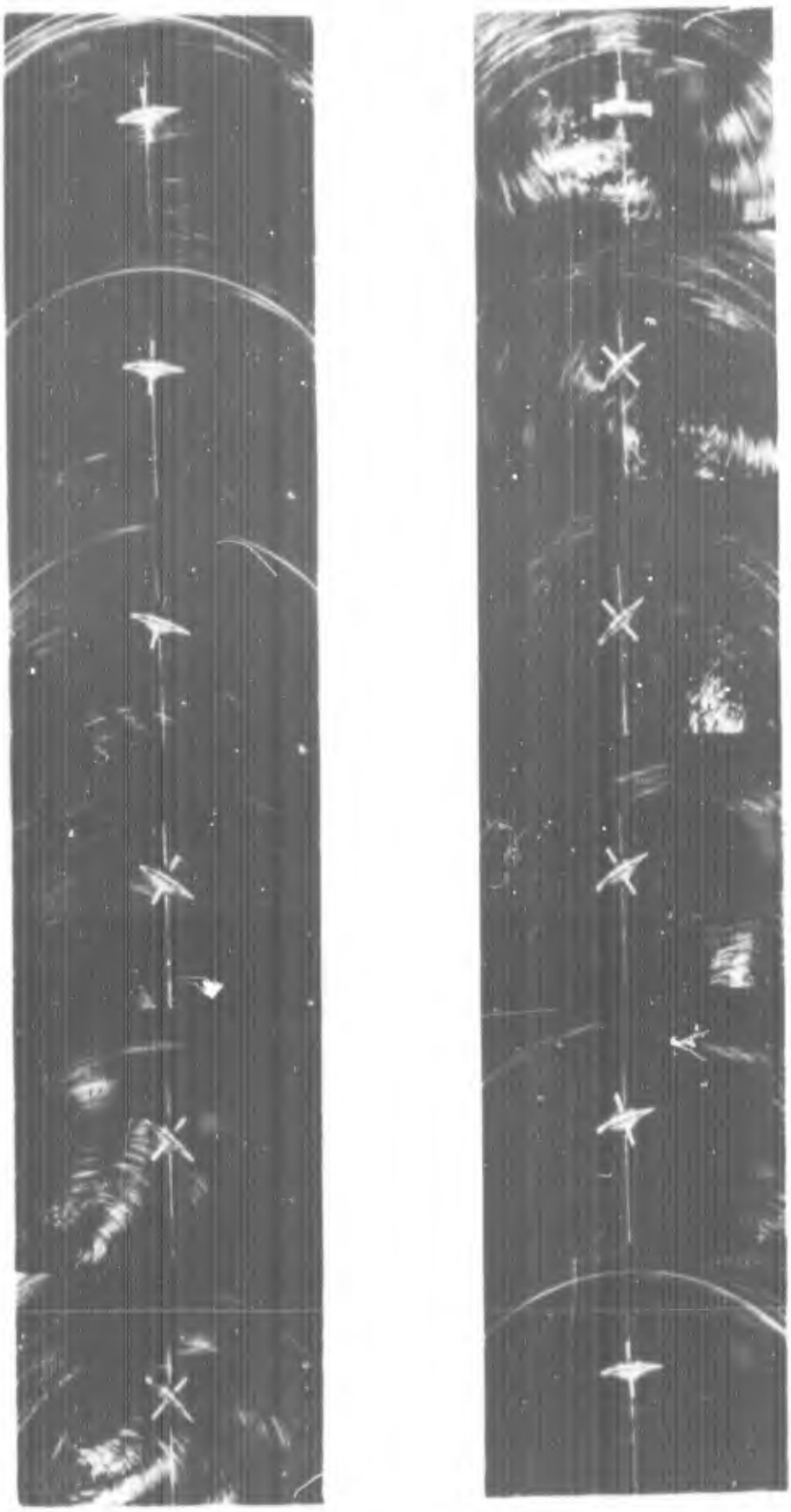

Figure 16 - One Cycle - V/ND = 0.5 - x/L = 0.5 - Radial Camera

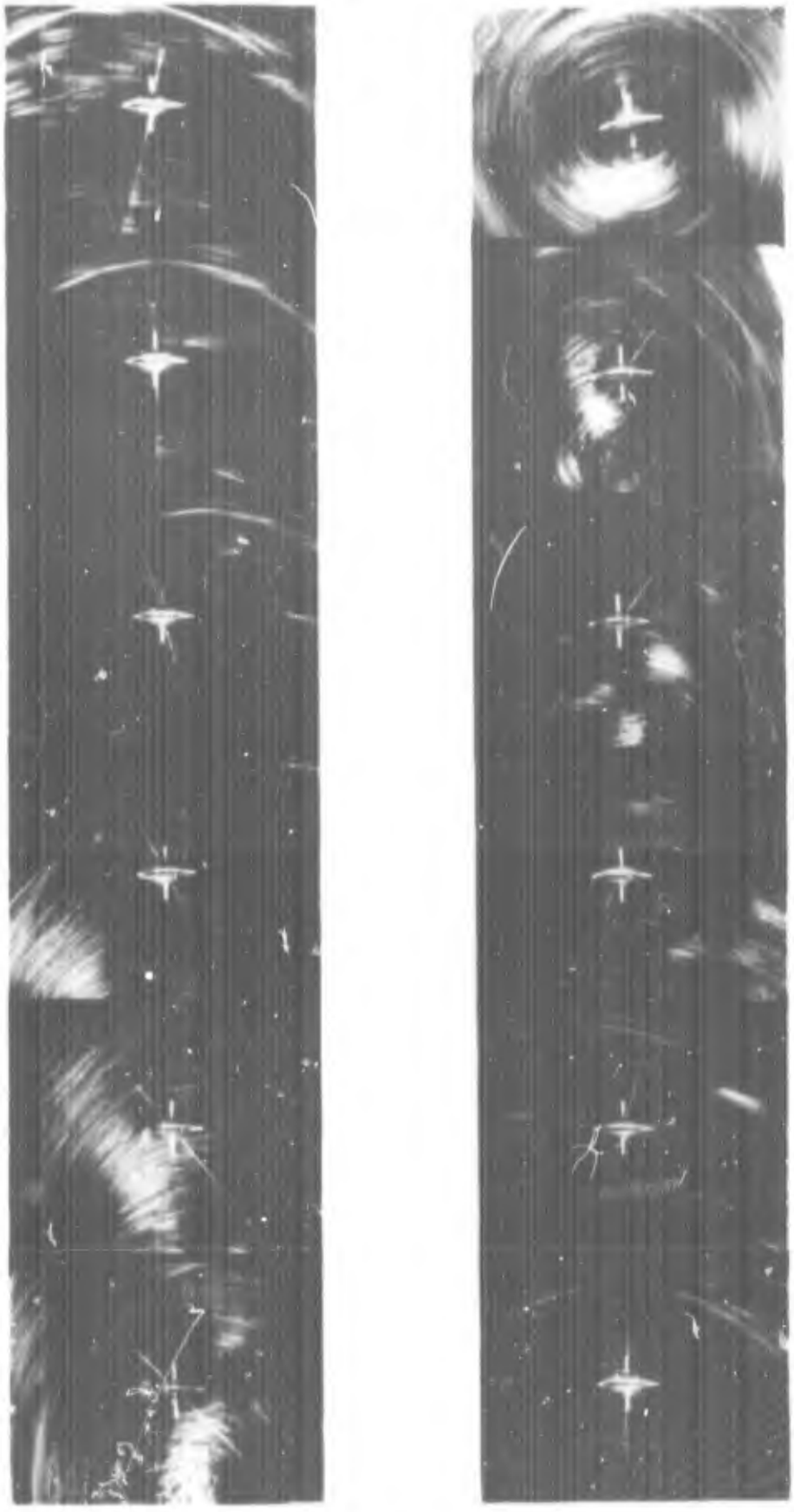

Figure 17 - One Cycle - V/ND = 0.5 - x/L = 0.5 - Articulated Camera

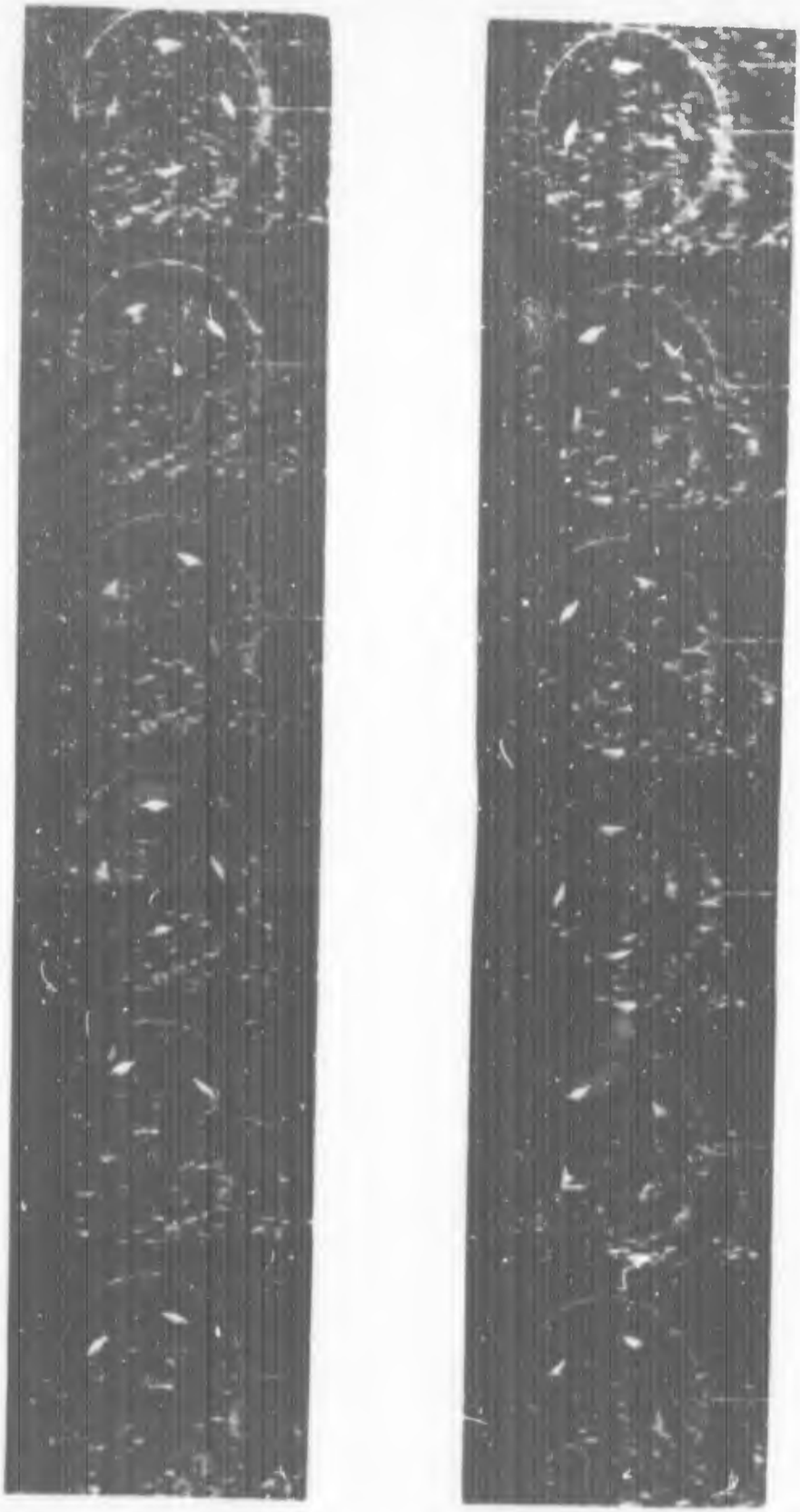

Figure 18 - One Revolution at V/ND = 1.75 - x/L = 0.5

Figure 19 - One Cycle - V/ND = 1.75 - x/L = 0.5 - Radial Camera

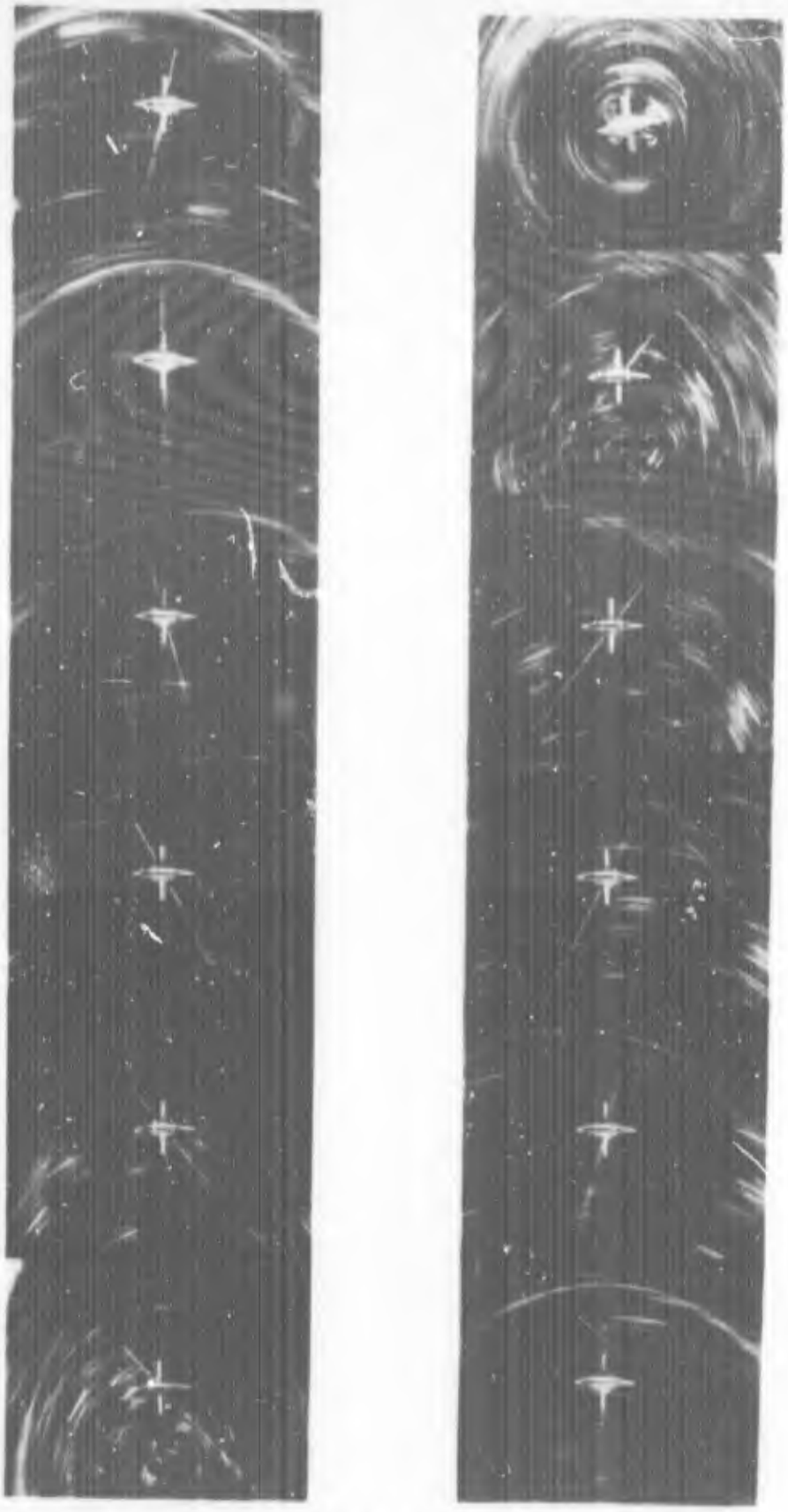

Figure 20 - One Cycle - V/ND = 1.75 - x/L = 0.5 - Articulated Camera